Scientific Report

of the Group of G. Weigelt

2002 — 2005

Young stellar objects, evolved stars, active galactic nuclei, infrared long-baseline interferometry, and theoretical studies

1 Young Stellar Objects: infrared interferometry and radiative transfer modeling of disks and outflows

Young stellar objects (YSOs) are typically surrounded by dense circumstellar material and often show strong outflow activity. The outflows are an essential ingredient of the star formation process as they are believed to contribute to the removal of excess angular momentum from accreted matter and to disperse infalling circumstellar envelopes. Despite their key role in star formation, the origin, acceleration, and collimation of the flows are still poorly understood.

We use *infrared bispectrum speckle interferometry* and *infrared long-baseline interferometry* to study the disks, jets, and outflows of young stellar objects of high- and intermediate mass. Considering complementary information from other wavelength regions, such as radio maps of molecular outflows or line emission from shocked H_2 gas, we derive physical models of the objects with the aid of *radiation transfer simulations.*

1.1 Is there a precessing jet in the massive protostellar outflow source IRAS 23151+5912?

The optically invisible infrared source IRAS 23151+5912 is a very luminous ($\sim 10^5\,L_\odot$), massive ($\sim 25\,M_\odot$) YSO at a distance of ~ 5.7 kpc. It exhibits a massive bipolar outflow with a dynamical age of only $\sim 20\,000$ years. Our reconstructed K-band bispectrum speckle interferometric image of IRAS 23151+5912 (Fig. 1 top left) reveals the diffuse nebulosity north-east of two point-like sources in unprecedented detail. A comparison of our image with mm continuum and CO molecular line maps showed that the brighter of the two point sources lies near the center of the mm peak, and that the near-infrared nebulosity *coincides very well with the blue-shifted CO outflow lobe.* This matches with the assumption that the outflow has cleared a cavity in the circumstellar material, and what we see as the diffuse nebulosity in our K-band image is a combination of $2.12\,\mu$m emission from shock-excited molecular hydrogen in the outflow and of light from the protostar that is scattered at the inner wall of this low-density outflow cavity or by material within the cavity. The red-shifted lobe of the outflow has probably cleared a similar cavity which is, however, pointing away from us and hidden from view in the near-IR by intervening disk extinction.

The most prominent feature of the diffuse nebulosity is a bow shock-like arc which, unlike the usual bow shocks in protostellar jets, points *towards* the source rather than away from

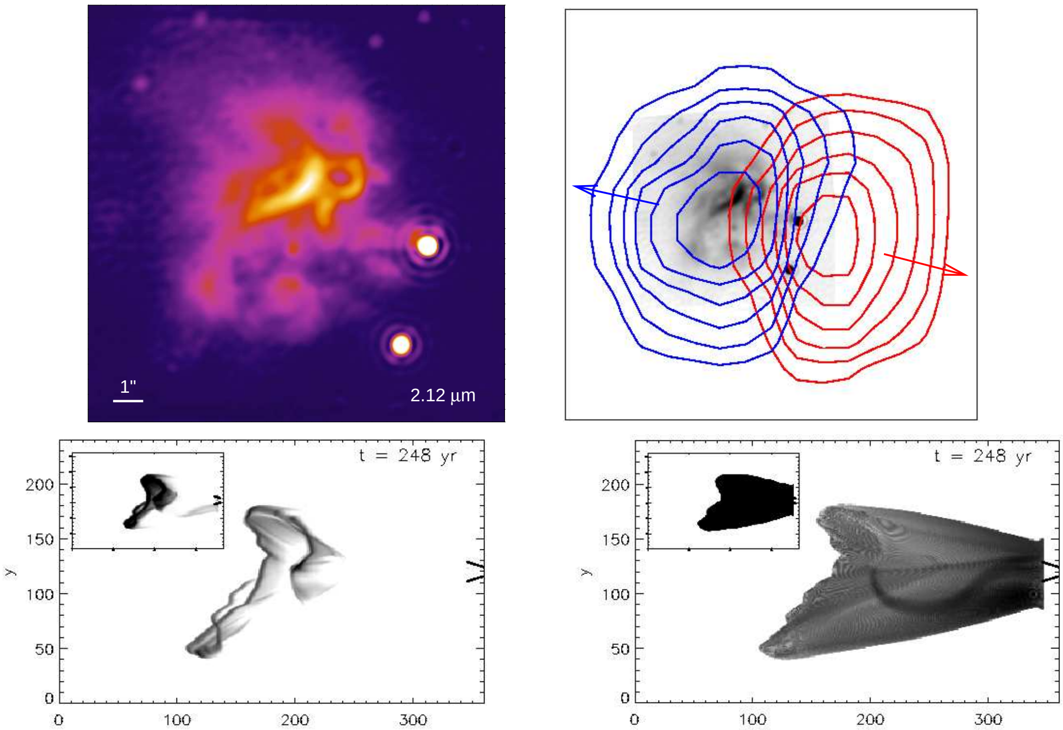

Figure 1: IRAS 23151+5912. **Upper Left:** Pseudocolor representation of our bispectrum speckle interferometry K-band image. **Upper Right:** Comparison of our K-band image (greyscale) to the CO line maps from Beuther et al. (A&A, 383, 892, 2002) shown as red and blue contours for the red- and blue-shifted CO emission. The direction of the outflow (PA $\sim$ 79°) is indicated by the arrows. **Lower Left:** Hydrodynamic simulation image of the 2.12 μm 1-0 S(1) line emission from molecular hydrogen resulting from a precessing jet. **Lower Right:** Simulated image of the CO J=2-1 emission at 230 GHz.

it. With numerical jet simulations (see Fig. 1, lower panels), we show that this structure can be understood assuming the action of a *precessing* jet on the ambient circumstellar material. The feature represents the remnant of the initial ring of shocked gas trapped within the volume of material swept up by the precessing jet. Our speckle image also reveals a linear structure connecting the central point source with the extended diffuse nebulosity. This linear structure seems to represent the innermost part of a jet that drives the strong molecular outflow (PA $\sim$ 80°) from IRAS 23151+5912. Our findings constitute a clear example for an apparently jet-driven outflow from a massive protostar and support the assumption of a common mechanism for the formation of outflows from protostars of all masses.

Complex structures are generally detected in the immediate circumstellar environments of intermediate- and high-mass protostars, and IRAS 23151+5912 is no exception. In Fig. 2 we show a mosaic of K-band bispectrum speckle interferometry images of several prominent intermediate- and high-mass protostars that have been studied by our group. The comparison shows that different objects display intriguingly different morphologies.

We have performed a large number of radiation transfer calculations of YSOs surrounded by envelopes and/or disks in order to better recognize the physical structure behind the features in the images. We applied the 2-D radiation transfer code described in Sonnhalter et al. (A&A, 299, 545, 1995), assuming a luminosity of 20 000 $L_\odot$ and an effective temperature of 30 000 K for the central source. We considered two different models: The first model is a dusty *envelope* with a radial power-law density distribution and low-density *outflow cavities*.

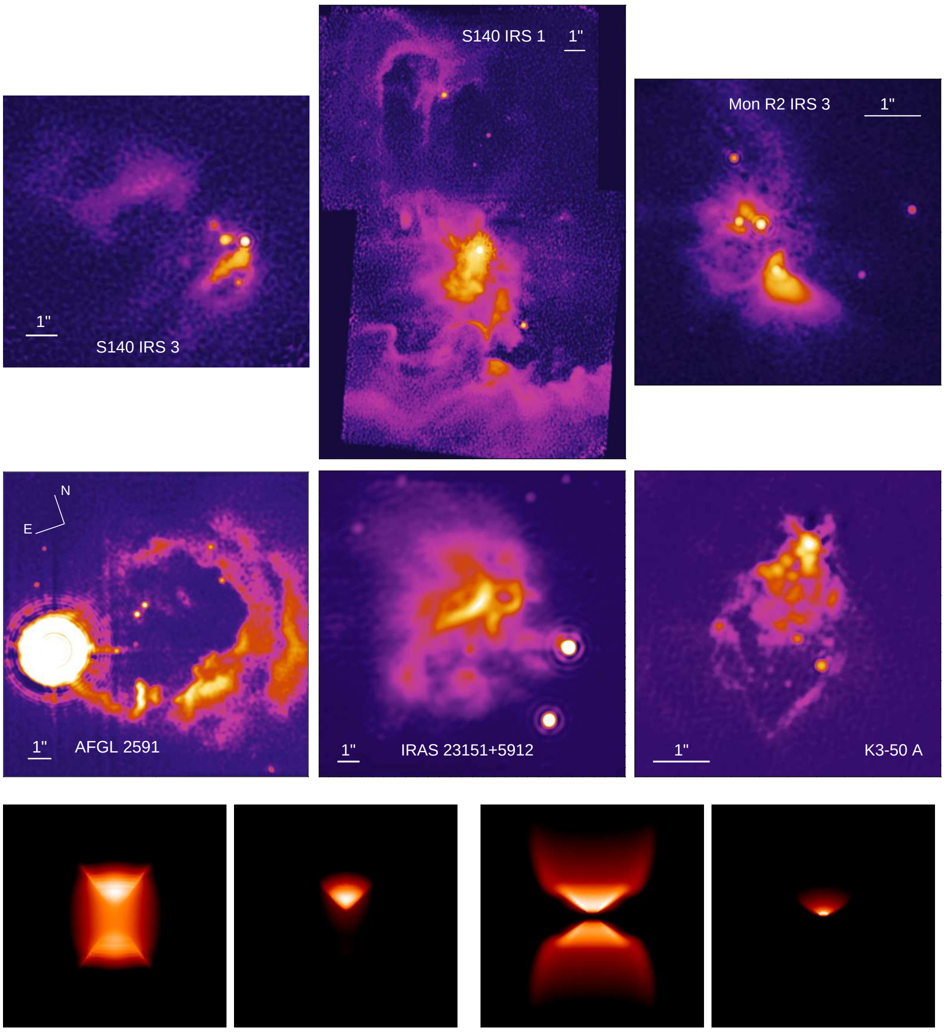

Figure 2: Comparison of K-band images from bispectrum speckle interferometry of several intermediate- and high-mass YSOs to radiation transfer simulations. **Upper two rows:** Pseudo-color representations of speckle reconstructions. The objects are arranged by increasing estimated luminosity. **Lower row:** simulated K-band images derived from 2-D radiative transfer calculations. The two left images correspond to a *spherical envelope model with cone-like cavities* (inclination angles of $i = 85°$ and $60°$), the two right images are from a model of a *disk embedded in a spherical halo with polar outflow cavities* ($i = 85°$ and $60°$). Each image shows a 1250×1250 AU region.

The second model assumes a geometrically thick *disk*, which is embedded in a spherical halo that has wind-blown *cavities*. Simulated K-band images for the two models with different inclination angles are shown in the lower row of Fig. 2. A common feature of the images is diffuse emission extending from the central point source with a fan-shaped morphology. The radiation transfer simulations demonstrate that the cone oriented towards us appears very bright for moderate inclination angles ($i \lesssim 75°$). For low inclination angles ($i \lesssim 60°$), the observer is able to look through the less dense regions of the cavities towards the hottest and, therefore, bright central regions. The opposite cone is considerably fainter or completely invisible because it is oriented away from us and hidden by circumstellar extinction. For high inclination angles ($i = 85°$, i.e. nearly edge-on) the direct view towards the central source is blocked, and the dominant features in the simulated images are scattering lobes above and below the disk or torus plane. Comparing the observed images to the radiative transfer simulations, we find that the objects showing fan-shaped morphologies are quite well reproduced with both models, seen under a rather high inclination angle. The small-scale clumpiness and bow-shocks cannot be simulated in our 2-D radiative transfer model, but were studied by hydrodynamical jet simulations (see Fig. 1).

→ Weigelt et al. (2006), A&A in press (astro-ph/0511178)

1.2 Peering into the heart of the high-mass star forming region K3-50 A

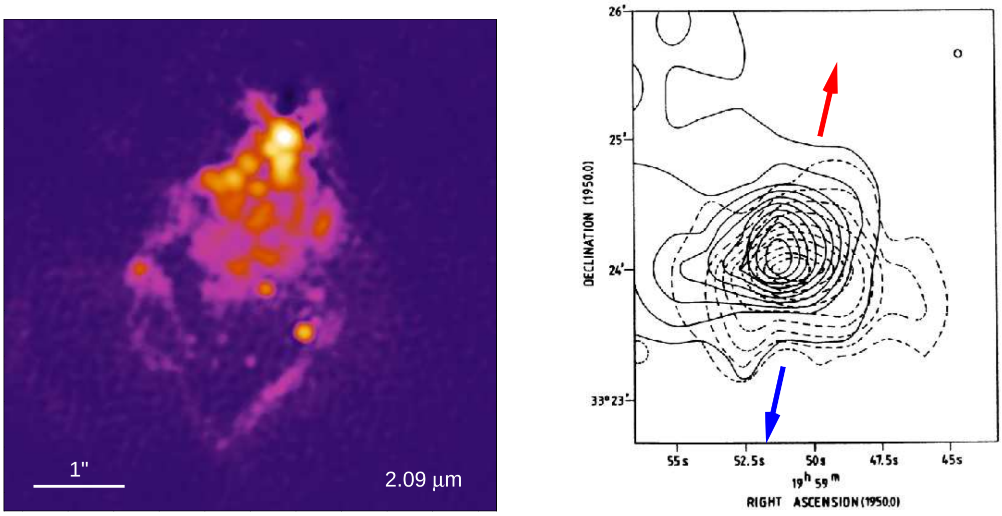

Figure 3: Left: Pseudocolor representation of our K-band bispectrum speckle interferometry image of K3-50 A. **Right:** CO map of K3-50 A from Phillips & Mampaso (A&AS, 88, 189, 1991), showing the large-scale molecular outflow. The arrows mark the outflow position angle of 160° determined by DePree et al. (ApJ, 428, 670, 1994).

The ultracompact H II region K3-50 A is known to be a site of massive star formation. In the past, it had been assumed that the central source of K3-50 A is a single, very massive ($M \sim 50\,M_\odot$) protostar. Recent observations, however, found a remarkable discrepancy between the Lyman continuum flux from K3-50 A, which corresponds to the expected output of a single O5.5V star, and the mid-infrared line-flux ratios, which suggest much later spectral types (O8-B0) for the ionizing stars. It was therefore suggested that K3-50 A is excited by at least two, possibly three ionizing stars. Our K-band bispectrum speckle interferometry image of K3-50 A (Fig.3) resolves the central $1'' \times 1''$ region into at least 7 point-like objects plus a fan-shaped nebula. The magnitudes of the other point-like sources indicate that some of them are also rather massive (probably early B-type) stars. This suggests that K3-50 A is a small cluster of high- to intermediate-mass stars. Our results demonstrate the importance of high spatial resolution observations for revealing the true nature of massive YSOs. The brightest K-band source is located exactly at the tip of the cone-shaped nebulosity and therefore also seems to be the dominant driving source of the molecular outflow. The nebula shows several arcs and the orientation of its main axis agrees very well with the direction of the CO outflow from K3-50 A. Therefore, this nebulosity very likely represents the clumpy inner surface of a partially evacuated cavity excavated by the strong outflow from the central massive protostar.

→ Hofmann et al. (2004) (see publication list of our institute for detailed references)

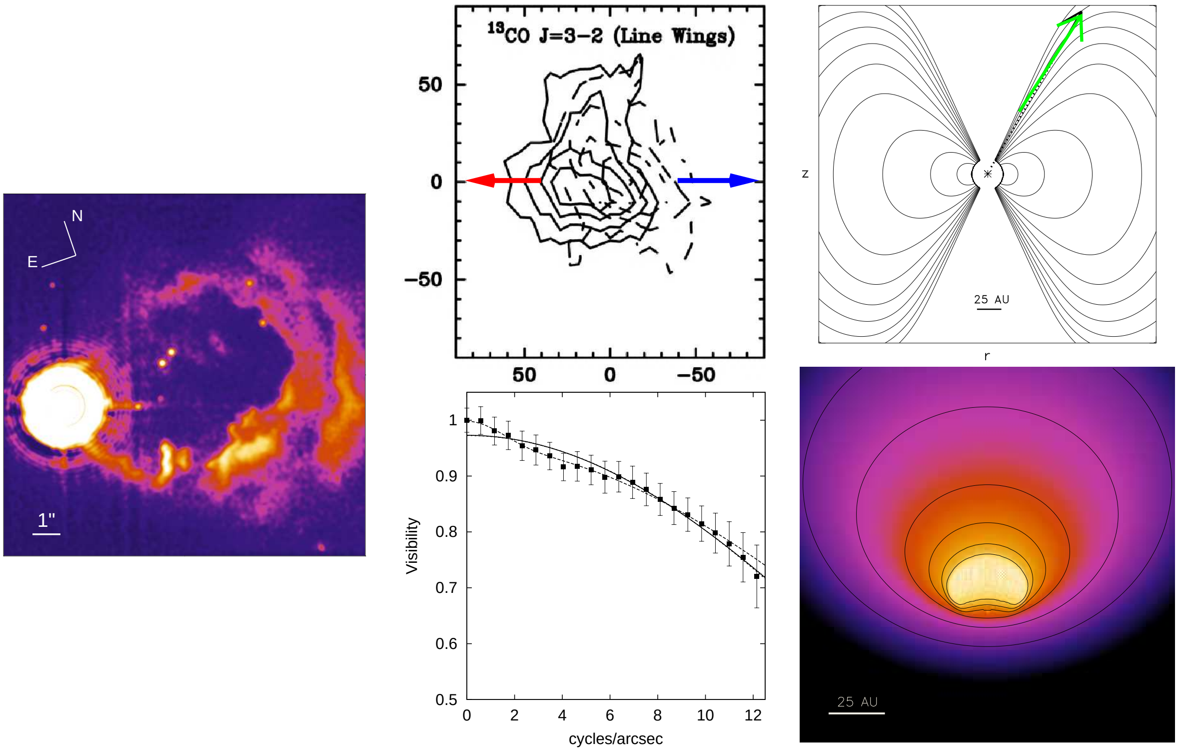

Figure 4: Left: Pseudocolor K-band bispectrum speckle image of AFGL 2591. **Upper Middle:** CO map of AFGL 2591 from van der Tak et al. (ApJ, 522, 991, 1999), showing (for comparison) the large-scale molecular outflow along position angle 270°. **Lower Middle:** Radial dependence of our azimuthally averaged K-band visibility of AFGL 2591, compared to the model visibilities of a two-component Gaussian disk model (dashed line) and of our radiation transfer simulation of a circumstellar disk model (solid line). **Upper Right:** Contour representation of the model density distribution. The green arrow shows the direction towards the observer ($i = 30°$). **Lower Right:** K-band model image resulting from the radiation transfer simulation of AFGL 2591. The bright white/yellow structure is the *inner irradiated wall* of the dusty disk near the *dust sublimation radius*.

1.3 Bispectrum speckle interferometry of the massive protostellar outflow source AFGL 2591

AFGL 2591 is an optically invisible infrared source in a massive star formation region in Cygnus. The luminosity of the source is $\sim 2 \times 10^4\,L_\odot$, suggesting a mass of about $10 - 15\,M_\odot$ for the young stellar object. AFGL 2591 drives a powerful bipolar molecular outflow with an extent of $\sim$ 1.5 pc in east-west direction (PA $\sim$ 270°) and a dynamical age of only 2×10^4 yrs. We have obtained a near-infrared K-band image of AFGL 2591 with a resolution of 170 mas using the bispectrum speckle interferometry method (Fig. 4 left). Our image shows the clumpy structure of the loops in unprecedented detail. While the rather broad loop shape suggests a wide outflow angle, other observations also revealed jet-like outflow activity around AFGL 2591. The loops may have been created by a wind-driven outflow component or by jet-like flows with a wide precession angle. The central protostellar source in AFGL 2591 is clearly resolved in our data. Analysis of the visibility (Fig. 4 lower middle) yields a uniform-disk diameter of $\sim$ 40 mas. In order to interpret this resolved structure, we performed 2-D radiation transfer simulations for a source surrounded by a geometrically thick disk (Fig. 4 right). Our simulated images suggest that the dominant structure in the K-band is the bright *inner wall* of a dusty disk at the *dust sublimation radius*. The size

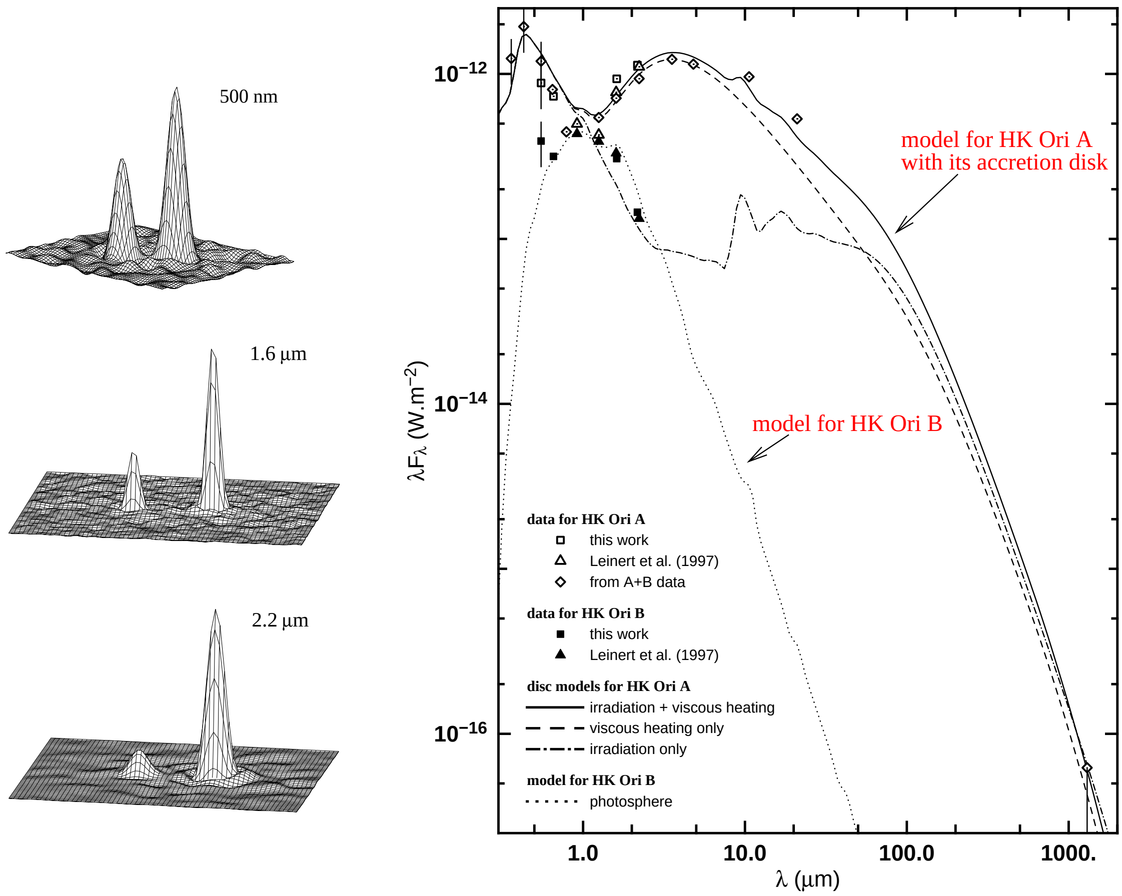

Figure 5: Left: Surface plots showing the brightness distribution in the bispectrum speckle images of HK Ori (separation ~ 0.3”) at 550 nm (top), 1.6 μm (middle), and 2.2 μm (bottom). **Right:** The observed SED of HK Ori’s components and model curves. For HK Ori A, a two-layer disk model including irradiation by the central star and heating by viscosity fits the data very well (solid line).

of the bright structure in our model image is $\sim 34 \times 24$ AU, and the model visibility fits the observed visibility quite well. This leads to the conclusion that the resolved structure in the speckle image corresponds to the inner rim of the circumstellar matter at the dust sublimation radius.

→ Preibisch et al. (2003)

1.4 Resolution of the close Herbig Ae binary HK Ori: decomposition of HK Ori’s SED into components B and A with its strong IR excess

We obtained optical and near-infrared diffraction-limited bispectrum speckle interferometry observations of the well-known Herbig Ae stars HK Ori, Elias 1, LkHα 198, V 380 Ori, and V 376 Cas. Bispectrum speckle interferometry of the individual components of HK Ori in four different wavelength bands between 550 nm and 2.2 μm allowed us to decompose the system SED into the two separate component SEDs (Fig. 5). The SED is clearly dominated by component A at wavelengths above $\sim 2\,\mu$m and also at wavelengths below $1\,\mu$m, whereas both components contribute similar fractions to the flux around $1\,\mu$m. The primary component A exhibits a strong infrared excess which suggests the presence of circumstellar material, whereas the companion can be modeled as a naked photosphere. The infrared excess of HK

Ori A contributes around two thirds of the total emission from this component and is much ($\sim 10\times$) stronger than seen in most other Herbig stars. The excess cannot be explained with irradiation of circumstellar matter by the central star but suggests that accretion power contributes significantly to the flux. The observed SED can be well reproduced with a radiative transfer model taking into account viscous disk heating by accretion. The modeling shows that a high accretion rate $\dot{M} = 2.5 \times 10^{-6}\, M_{\odot}/\mathrm{yr}$ is required to fit the SED. HK Ori is probably in a transitory high-accretion state.

→ Smith et al. (2004), Smith et al. (2005)

1.5 Mid-infrared interferometry with the MIDI instrument of ESO's Very Large Telescope Interferometer: first spectro-interferometric measurement of the mid-infrared sizes of circumstellar disks around Herbig Ae/Be stars in the wavelength range of $8 - 13\,\mu$m

The MIDI instrument of the European Southern Observatory's (ESO) Very Large Telescope Interferometer (VLTI) on Cerro Paranal combines the light of two 8.2 m telescopes and provides spectrally dispersed visibilities in the $8 - 13\,\mu$m atmospheric window. It traces the emission from hot and warm dust in the inner disk regions of young stellar objects and can be used to constrain the geometrical structure of the circumstellar material on angular scales of ~ 20 mas (for a 100 m baseline), corresponding to spatial scales of a few AU at the distance of the nearest young stellar objects. The first MIDI observations of young stellar objects were used to study circumstellar disks surrounding seven nearby Herbig Ae/Be stars (baselines between 74 m and 102 m; see Fig. 6)

The N-band spectra of the targets are shown in the upper panel of Fig. 7. They show a wide range of different features and can be used for a compositional analysis of the circumstellar dust. The spectrally resolved mid-infrared visibilities measured with MIDI are shown in the lower panel of Fig. 7. All targets were resolved, and the characteristic dimensions of the emitting regions at 10 μm were found to be in the range of 1 AU to 10 AU (see Fig. 7). The 10 μm sizes of the sample stars correlate with the slope of the $10 - 25\,\mu$m infrared spectrum in the sense that the reddest objects are the largest ones. Such a correlation would be consistent with a different geometry in terms of flaring or self-shadowed flat disks for sources with strong or moderate mid-infrared excess, respectively. In Fig. 7 the observed spectrally resolved visibilities were compared with predictions based on existing models of passive, centrally irradiated hydrostatic disks with an inner hole and a puffed-up inner rim at the dust sublimation radius (Dullemond et al., ApJ, 560, 957, 2001) made to fit the SEDs of the observed stars. While there is broad qualitative agreement of the spectral shape of visibilities corresponding to these models with our observations, there are significant quantitative discrepancies that emphasize the importance of interferometry for the modeling of circumstellar disks.

→ Leinert et al. (2004)

1.6 Revealing the building blocks of planets within the 'terrestrial' region of protoplanetary disks with MIDI/VLTI mid-infrared interferometry

MIDI observations can provide new insights into the spatial variations of the dust composition in the circumstellar material surrounding young stellar objects. The first spatially resolved

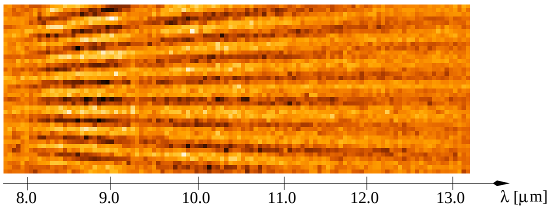

Figure 6: Spectrally dispersed N-band interferograms of the Herbig Ae/Be star 51 Oph obtained with the VLTI/MIDI instrument.

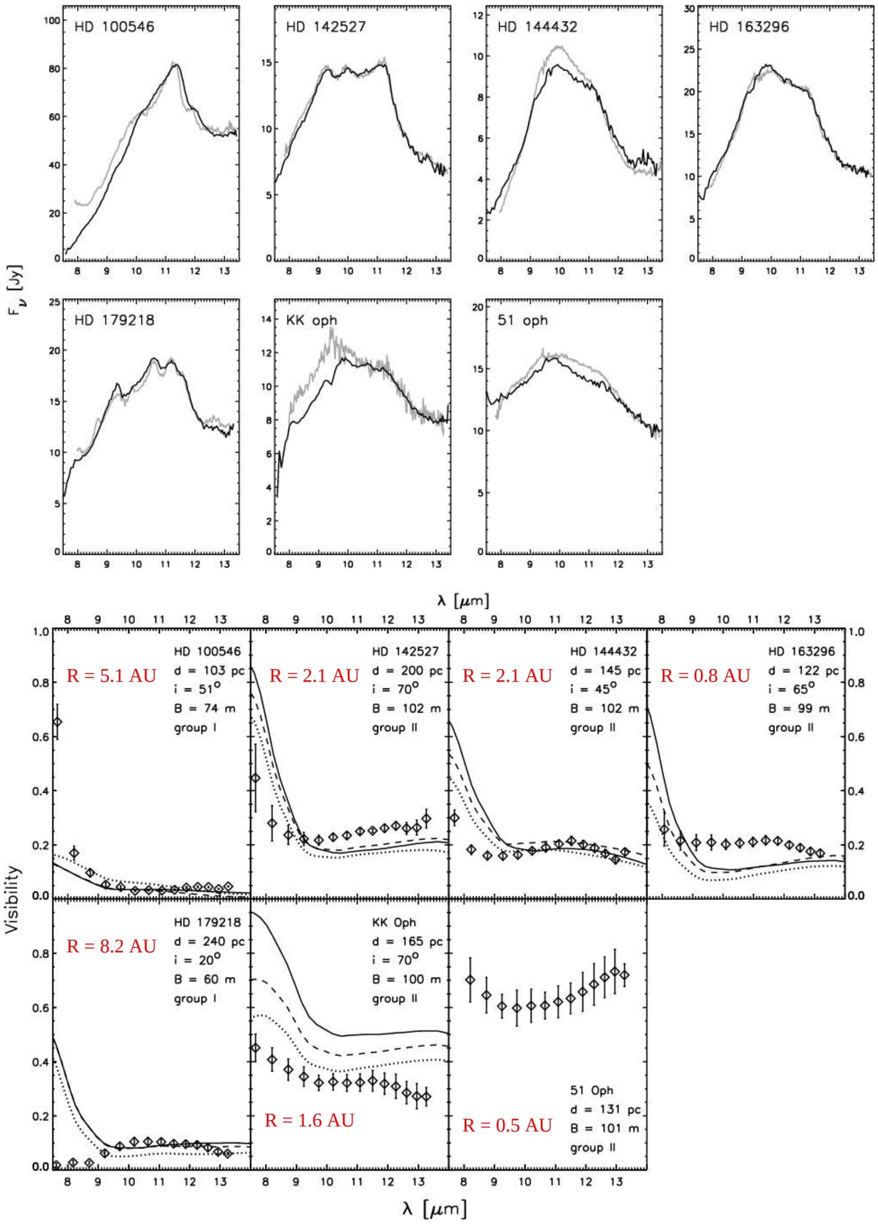

Figure 7: Top: Observed $7.5 - 13.5\,\mu$m spectra of the seven Herbig Ae/Be stars observed with the MIDI interferometry instrument at the VLTI. Note the large range in silicate band shapes and the presence of crystalline silicates (shoulder at $11.3\,\mu$m) in some objects. PAH bands at 7.9, 8.6 and $11.3\,\mu$m are prominent in HD 100546 and HD 179218. The MIDI spectra are indicated in black, and grey lines indicate spectra obtained with TIMMI 2. **Bottom:** The observed MIDI/VLTI visibilities of the seven Herbig Ae/Be stars (diamonds with error bars). The radii R derived for each object are displayed in red. The lines show model predictions for circumstellar disks around these stars based solely on the SEDs. Three model visibility curves are shown: two referring to the inclination used in the SED fitting and calculated for a cut along the long axis (broken line) and along the short axis (solid line), respectively, while the dotted line is the prediction for a pole-on view.

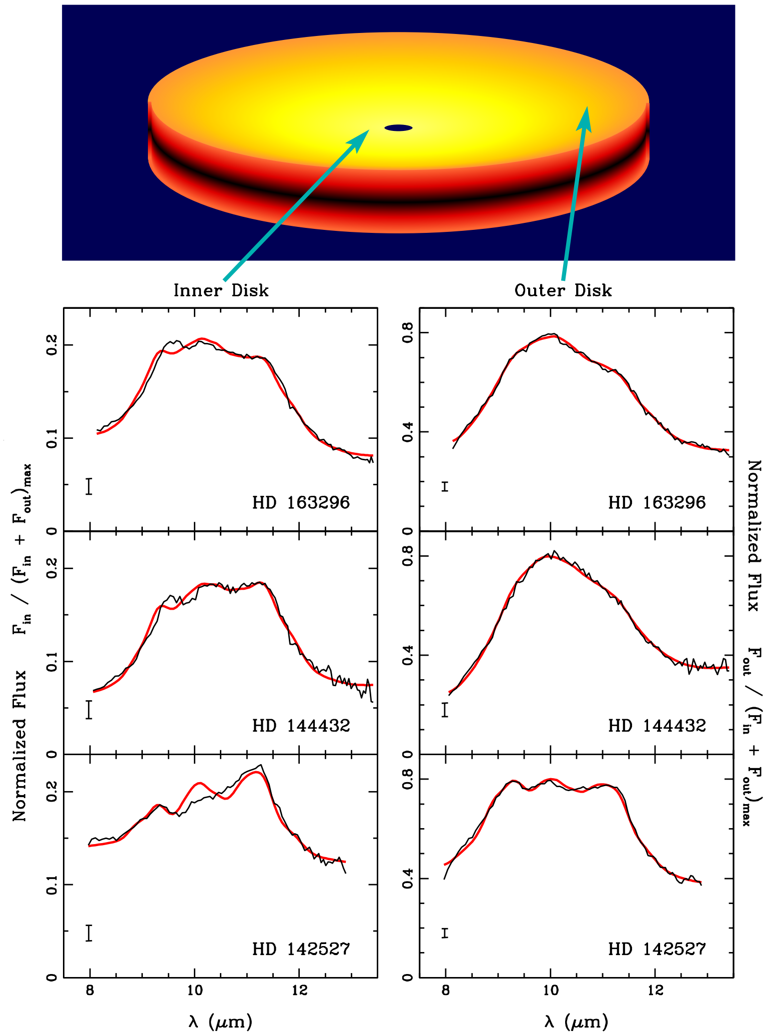

Figure 8: MIDI mid-infrared interferometry of the three Herbig Ae stars HD 163296, HD 144432, and HD 142527: Infrared spectra of the (left) inner (1 − 2 AU) and (right) outer (2 − 20 AU) disk regions. Note the different shapes of the 10 μm silicate features in the inner and outer parts of the disks, providing strong evidence for differences in the dust composition in the inner and outer disk regions (red lines: models; black lines: observations).

compositional analysis of circumstellar dust of Herbig Ae/Be stars was performed with MIDI observations that combined the light from two of the 8.2 m VLTI telescopes with baselines around 100 m. Although most of the dust mass in the cloud from which our Solar System was formed is contained in amorphous silicates, crystalline silicates are abundant throughout the Solar System, reflecting the thermal and chemical alteration of solids during planet formation. The evolution of the dust that forms Earth-like planets is still very poorly understood. MIDI has now allowed us to perform spatially resolved detections and compositional analysis of these building blocks in the innermost two astronomical units of three proto-planetary disks. The MIDI data allowed us to reconstruct the $8 - 13\,\mu$m spectra of the inner ~ 2 AU regions of these disks and the corresponding spectra of the outer disk regions (Fig. 8). The dust in these inner regions was found to be *highly crystallized*, more so than any other dust observed in young stars until now. In addition, the outer region of one star has equal amounts of pyroxene and olivine, whereas the inner regions are dominated by olivine. The spectral shape of the inner-disk spectra shows surprising similarity with Solar System comets. Radial-mixing models naturally explain this resemblance as well as the gradient in chemical composition. These observations imply that silicates crystallize before any terrestrial planets are formed, which is consistent with the composition of meteorites in the Solar System.

→ van Boekel et al. (2004)

1.7 First near-infrared (2.2 μm) spectro-interferometry with ESO's Very Large Telescope Interferometer: AMBER interferometry of the Herbig Be star MWC 297

AMBER is the near-infrared three-telescope beam combiner of ESO's Very Large Telescope Interferometer (VLTI). This instrument was designed and built by an international consortium of groups at the university of Nice, the university of Grenoble, the Arcetri observatory in Florence, and the MPIfR. AMBER is currently the only near-infrared interferometric instrument which can record spectrally dispersed interferograms. It was installed at Paranal in March 2004 and commissioned in 2004 and 2005.

One of the first targets which has been observed with AMBER using two 8.2 m telescopes of the VLTI was the young stellar object MWC 297, an embedded B1.5Ve star exhibiting strong hydrogen emission lines and a strong near-infrared continuum excess. MWC 297 has been spatially resolved in the continuum with a visibility of $0.50^{+0.08}_{-0.10}$. In the Brackett gamma (Brγ) emission line the visibility decreases to a significantly lower value of 0.33 ± 0.06. This change in the visibility with wavelength can be interpreted as the presence of both an optically thick disk responsible for the visibility in the continuum and an extended stellar wind traced by the Brγ emission line, leading to a 40% increase of the apparent size.

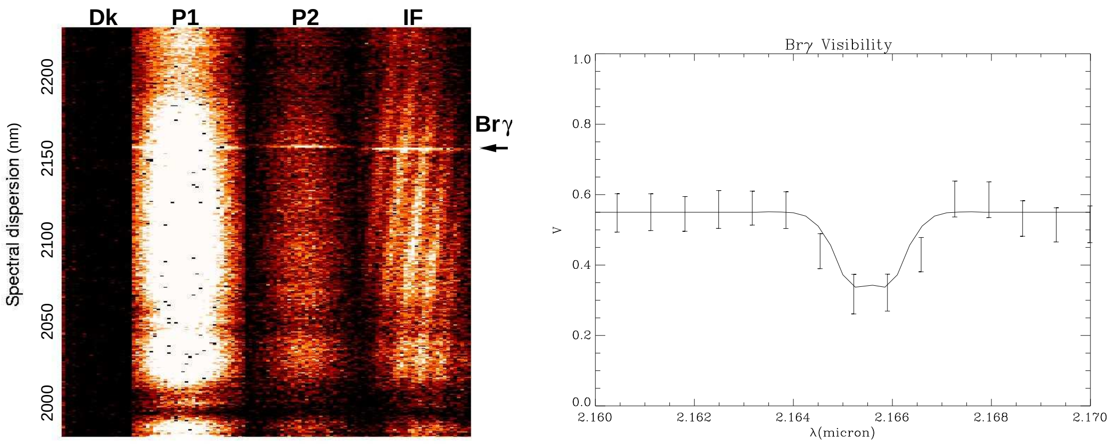

Figure 9: Left: Short-exposure image of the MWC 297 signal on the AMBER detector. The x-axis corresponds to the spatial extension of the beams and the y-axis to the wavelength. First column (Dk) corresponds to the dark current, and the second (P1) and third (P2) columns are the beams from the first and second telescope, respectively. The last column (IF) shows the fringes obtained by superposition of the two 8.2 m telescope beams. The bright horizontal structure is the Brγ line at 2.165 μm. **Right:** The visibility observed with AMBER (with error bars, spectral resolution 1500) and the one obtained from the outflowing wind model (solid line).

We validated this interpretation by building a model of the stellar environment that combines both a geometrically thin, optically thick accretion disk consisting of gas and dust, and a latitude-dependent stellar wind. Our disk+wind model yields an inclination of the system of approximately 20°. Our model suggests that MWC 297 is surrounded by an equatorial flat disk that is possibly still accreting and an outflowing wind which has a much higher velocity in the polar region than at the equator. The VLTI/AMBER unique capability to measure spectral visibilities therefore allows us, for the first time, to compare the geometry of a wind with the disk structure in a young stellar system.

$\rightarrow$ Malbet et al. (2006), A&A in press (astro-ph/0510350)

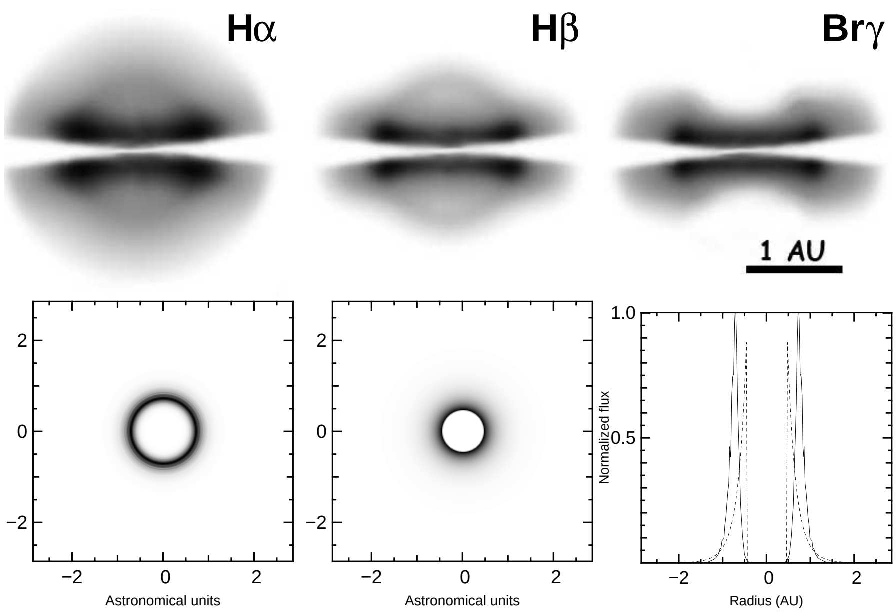

Figure 10: Top: Edge-on model intensity maps of the wind in the Hα, Hβ, and Brγ lines of MWC 297. **Bottom:** Pole-on intensity maps of the Brγ wind emission (left panel) and of the K-band disk continuum emission (center panel). The right panel shows a radial cut of these intensity maps.

1.8 X-ray Observations of YSOs: The "Chandra Orion Ultradeep Project"

The "Chandra Orion Ultradeep Project" (COUP), a 10 day long observation of the Orion Nebula Cluster (ONC) with the Chandra X-ray observatory, represents, by far, the deepest X-ray observation ever made of a young stellar cluster. The COUP image (see Fig. 11) shows 1616 individual sources in the $17' \times 17'$ field of view. COUP provides X-ray data on a sample of ~ 600 optically well-characterized T Tauri stars (TTS), more than 95% of which are detected as X-ray sources. A comprehensive study of their X-ray properties shows that solar-type coronal loops are probably the dominant source of the observed X-ray emission and suggests that the ultimate origin of the X-ray activity is most likely a turbulent dynamo working in the stellar convection zone. While the X-ray activity of the non-accreting TTS is consistent with that of rapidly rotating main-sequence stars, the accreting stars are less ($\sim 2\times$) X-ray active and show larger scatter in the correlations of X-ray and stellar parameters. This effect may be related to changes of the coronal structure or the internal stellar structure induced by the accretion process.

COUP also detected X-ray emission from nine of the spectroscopically-identified brown dwarfs in the ONC. The X-ray properties of the brown dwarfs are similar to those of the low-mass stars in the ONC and also to those of field stars of similar spectral types. This suggests that the key to the magnetic activity in very cool objects is not their mass, but their effective temperature, which determines the degree of ionization in the atmosphere.

The O- and early B-type stars in the ONC show the rather constant soft X-ray emission as expected from models of radiatively driven stellar wind shocks, but most of them also exhibit harder X-ray emission and/or flare-like variability. This strongly supports the idea that magnetic fields are an important ingredient for the generation of X-ray emission in hot stars. The observed properties of the late B- and A-type stars, on the other hand, are consistent with the idea that these intermediate-mass stars are not intrinsic X-ray emitters;

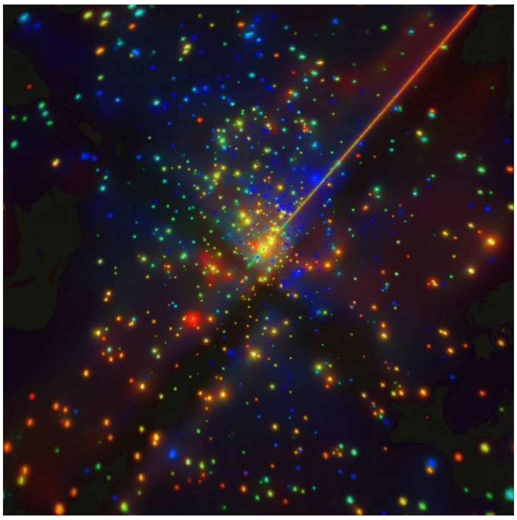

Figure 11: True-color X-ray image of the Orion Nebula Cluster obtained in the "Chandra Orion Ultradeep Project", showing the central $\sim 10' \times 10'$ region. The $0.2-1.0$ keV emission is shown in red, the $1-2$ keV emission in green, and the $2-8$ keV emission in blue.

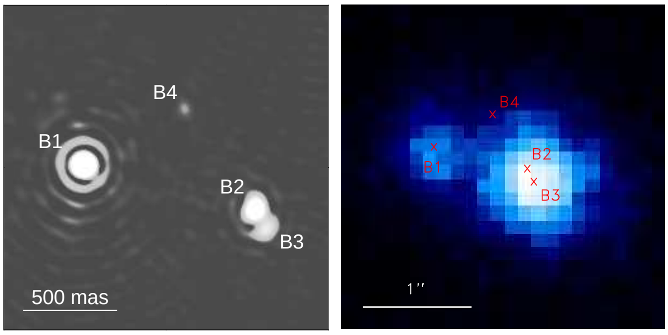

Figure 12: Left: K-band bispectrum speckle image of the θ^1 Ori B multiple system.
Right: Chandra $0.5-8$ keV X-ray image of the θ^1 Ori B multiple system based on the COUP data. The positions of the components B1 to B4 are shown by crosses and labeled.

some of them actually remained undetected, and the X-ray detected objects exhibit X-ray flares and have luminosities that are consistent with magnetic activity from known or yet unknown low-mass companions.

A good example for the X-ray properties of high- and intermediate-mass stars is the θ^1 Ori B multiple system. Our previous speckle observations (Schertl et al., A&A, 402, 267, 2003) resolved θ^1 Ori B into four visual components, B1 to B4, all located within $1''$ of each other (Fig. 12 left). The primary component B1 is of spectral type B3, components B2 and B3 are presumably intermediate-mass stars with spectral types in the range between A5 and F9, while B4 is a low-mass object. The Chandra image (Fig. 12 right) clearly resolves the X-ray emission from θ^1 Ori B into contributions from components B1 and B2/B3, while the close B2–3 pair ($\rho \sim 205$ mas) remains unresolved. The early B-type star B1 produces rather constant X-ray emission with a fractional X-ray luminosity of $\log(L_X/L_{\rm bol}) = -6.8$, which is dominated by a soft 7×10^6 K plasma component, i.e. has properties typical for wind shock related X-ray emission from massive stars. The X-ray emission from B2/B3, on the other hand, shows strong flaring variability with a mean fractional X-ray luminosity of $\log(L_X/L_{\rm bol}) \sim -4$ and is dominated by a hard 6×10^7 K plasma component. These properties are typical for coronal activity of late type stars and suggest that either B2 or B3 is probably a magnetically active F star. If the X-ray emission from B1 and B2/B3 were not resolved, one would infer an apparent fractional X-ray luminosity of $\log(L_X/L_{\rm bol}) \sim -5.4$ for the early B-type star, very similar to values observed for other, less well investigated B- and A-type stars. The X-ray data therefore support the suggestion, based on our infrared speckle studies, that most (if not all) B- and A-type stars are multiple systems.

→ Preibisch et al. (2005a), Preibisch et al. (2005b), Preibisch et al. (2005c), Feigelson et al. (2005), Getman et al (2005), Stelzer et al. (2005)

2 Stars in late evolutionary stages

2.1 Near-infrared speckle interferometry and phase-dependent radiative transfer modeling of the OH/IR star OH 104.9+2.4 using the DUSTY code

We obtained K'-band ($\lambda = 2.13\,\mu$m) visibilities from speckle-interferometric observations of the highly dust-enshrouded OH/IR star OH 104.9+2.4 with the SAO 6 m telescope in Sep. 2002 and Oct. 2003. The diffraction-limited resolution of 74 mas was attained. No major deviation of the circumstellar dust shell from spherical symmetry could be detected. The goal of our study was to carry out 1-D radiative transfer calculations using the code DUSTY (Ivezic & Elitzur, ApJ, 445, 415, 1995) to *simultaneously* model both the K'-band visibilities and the SED of OH 104.9+2.4 measured at two different epochs. Using these multi-epoch observations for our radiative transfer modeling, we were able to determine the temporal change of physical parameters of the circumstellar environment as a function of the variability phase of the source. The observations of OH 104.9+2.4 in Sep. 2002 and Oct. 2003 (see Fig. 13, top right panel), correspond to phases 0.0 and 0.25, respectively.

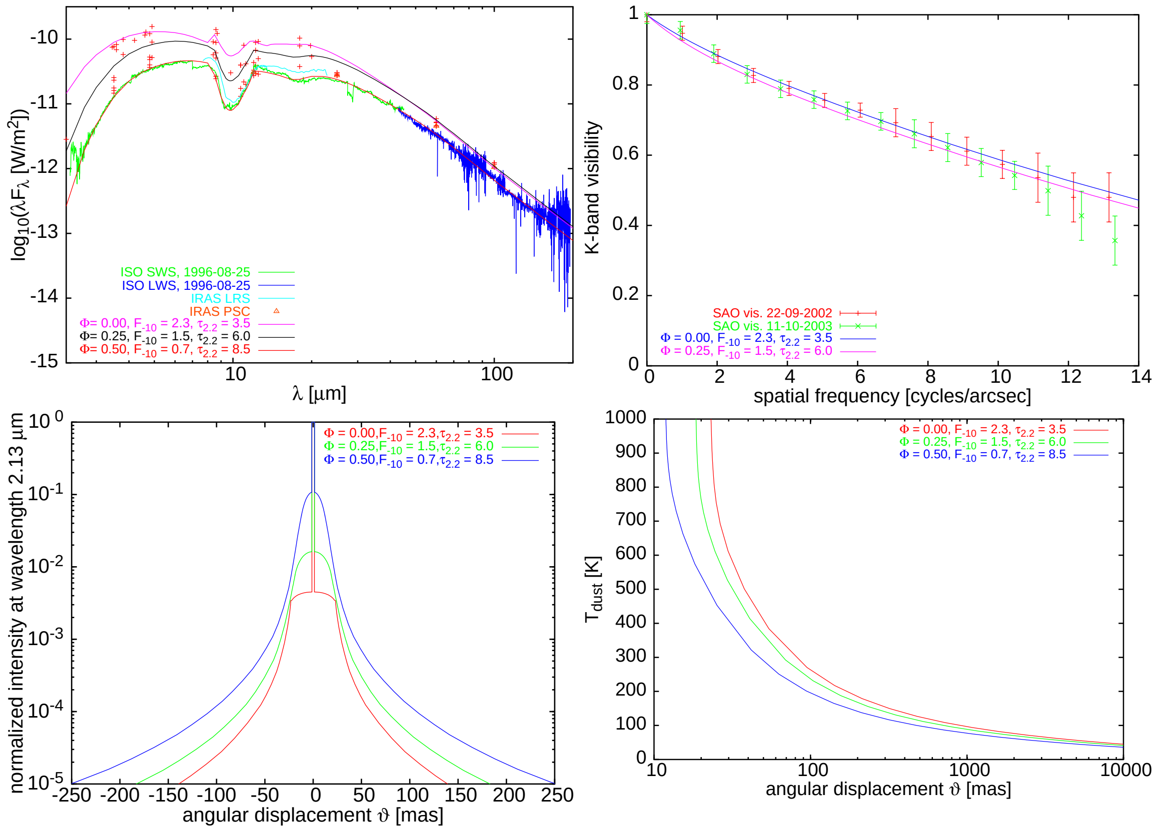

Figure 13: Top: Comparison of SED (**left**) and K' visibility (**right**) from our best-fitting model with photometric data and our SAO 6 m telescope visibilities of OH 104.9+2.4. Different bolometric flux values have been used for the SED and visibility model in order to account for the different epochs/phases of the observations. **Bottom**: Normalized K'-band intensity profile (**left**) and radial dust temperature profile (**right**) of our best-fitting model for phases 0.0 (=maximum phase), 0.25, and 0.5. The sharp central peak in the intensity profile corresponds to the central source of radiation. In the temperature profile, the point where $T_{\rm dust} = 1000\,$K indicates the inner radius of the dust shell. As the figure shows, due to the variability of the central source, the inner dust shell boundary moves from 11.9 mas (=8.3 $R_\star$) to 23.1 mas (=17.5 $R_\star$) between minimum and maximum pulsation phase.

From our radiative transfer modeling of OH 104.9+2.4, we found that due to the strong variability, the temperature of the central source increases by as much as ~ 900 K from minimum to maximum phase while the stellar radius decreases by $\sim 55R_\odot$ (= 8%). Correspondingly, the luminosity increases by a factor of ~ 3.3, leading to an outward shift of the inner dust shell boundary from 8.3 to 17.5 $R_\star$ due to strong dust evaporation. In Fig. 13 (lower right panel), this remarkable change is illustrated by the corresponding changes of the dust temperature profile. The left panel of Fig. 13 shows the corresponding change of the shape of the K'-intensity profile as a function of phase. In addition, we found from our best model that between minimum and maximum of the variability cycle, the optical depth in the 10 μm regime drops by a factor of ~ 2.4 and the gas mass-loss rate increases by nearly a factor of two from $\dot{M} \approx 3.1 \times 10^{-5}\, M_\odot \mathrm{yr}^{-1}$ to $\dot{M} \approx 5.7 \times 10^{-5}\, M_\odot \mathrm{yr}^{-1}$. Our study of OH 104.9+2.4 illustrates the importance of both multi-epoch observations and radiative transfer modeling in order to determine the phase-dependent physical properties of the circumstellar environment of highly variable, evolved stars at the end of their AGB evolution.

→ Riechers et al. (2004), Riechers et al. (2005)

2.2 Bispectrum speckle interferometry and 2-D radiative transfer modeling of the bipolar outflow of the AGB star CIT 3 using the code LELUYA

The transition from spherically symmetric Asymptotic Giant Branch (AGB) winds to non-spherical Planetary Nebulae (PNe) represents one of the most intriguing problems of stellar astrophysics. We revisited our observational results of the oxygen-rich AGB star CIT3 (=IRC+10011) obtained by Hofmann et al. (A&A, 379, 529, 2001) who discovered distinct asymmetries in the circumstellar envelope of this highly evolved AGB star (see top panels in Fig. 15). In our new study, we carried out detailed 2-D radiative transfer modeling of CIT 3 using the code LELUYA which successfully explains the observed asymmetries.

A comparison between observed and modeled visibilities along the major and minor symmetry axis is shown in Fig. 14 for $\lambda = 1.24, 1.65, 2.12$, and 11 μm, while Fig. 15 illustrates the comparison of observed and modeled J-, H-, and K'-band images. As Fig. 15 reveals, the overall image asymmetry is much more prominent in the J band, where dust scattering dominates the radiative transfer. As the wavelength shifts toward dominance of dust thermal emission, the image becomes more symmetric. Our radiative transfer modeling suggests that the image asymmetries originate from swept-up wind material in an elongated cocoon, whose expansion is very likely driven by bipolar jets. We performed our radiative transfer calculations with the cocoon modeled as two cones extending to $\sim 1,000$ AU within an opening angle of $\sim 30°$, imbedded in a wind with the standard r^{-2} density profile (see the model geometry illustrated in Fig. 14). Similar bipolar expansions, at various stages of evolution, have recently been observed in a number of other AGB stars culminating in jet breakout from the confining spherical wind. The bipolar outflow is triggered at a late stage in the evolution of AGB winds, and CIT 3 provides its earliest example thus far. These new results enable us to study the first instance of symmetry breaking in the evolution from AGB to planetary nebula.

→ Vinkovic et al. (2004)

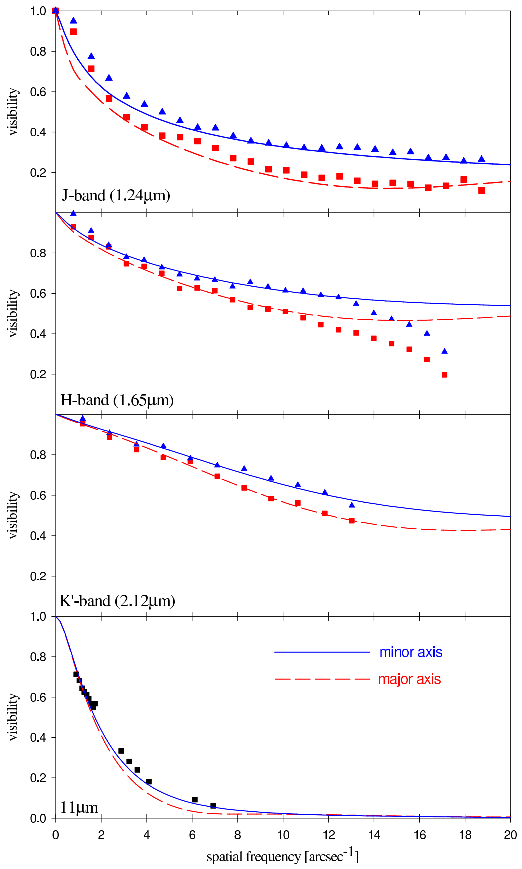

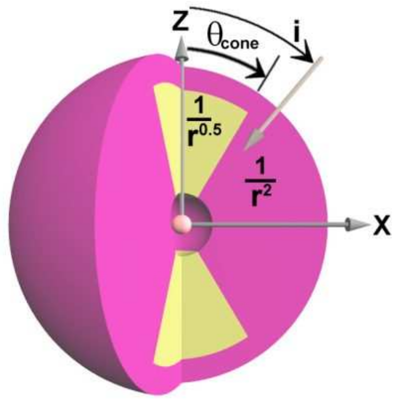

Figure 14: Left: Theoretical and observational visibility functions of CIT3. Solid and dashed lines are model predictions for cuts along the major and minor symmetry axis, respectively, and symbols are data points taken from Hofmann et al. (2001) (near-IR) and Lipman et al. (ApJ, 532, 467, 2000; 11 μm). **Top**: Sketch of our 2-D model. In a spherical wind with the standard $1/r^2$ density profile two polar cones are imbedded with half-opening angle $\theta_{\rm cone}$ and a $1/r^{0.5}$ density profile. The system is viewed from angle i to the axis.

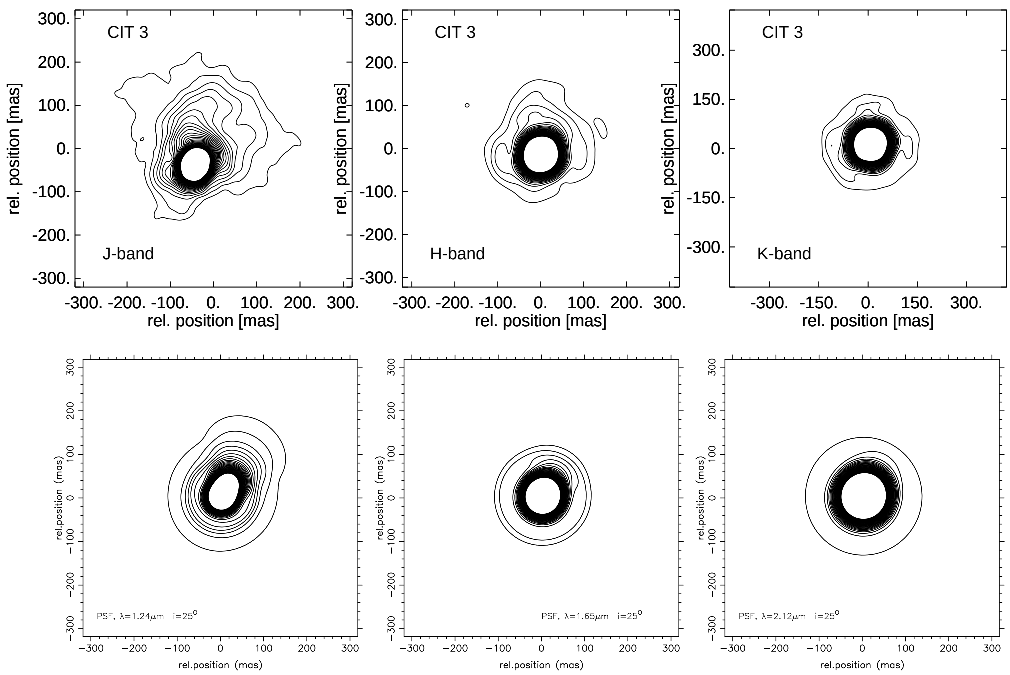

Figure 15: J-band (1.24 μm), H-band (1.65 μm), and K'-band (2.12 μm) images of CIT 3. Top row: Images obtained from bispectrum speckle interferometric measurements by Hofmann et al. (2001). Lower row: Theoretical LELUYA images. The transition from scattered light dominance in the J band to thermal dust emission in the K' band creates a sudden disappearance of the image asymmetry.

2.3 First mid-infrared (8–13 μm) spectro-interferometry of an evolved star with the VLTI/MIDI instrument: the Mira variable RR Sco

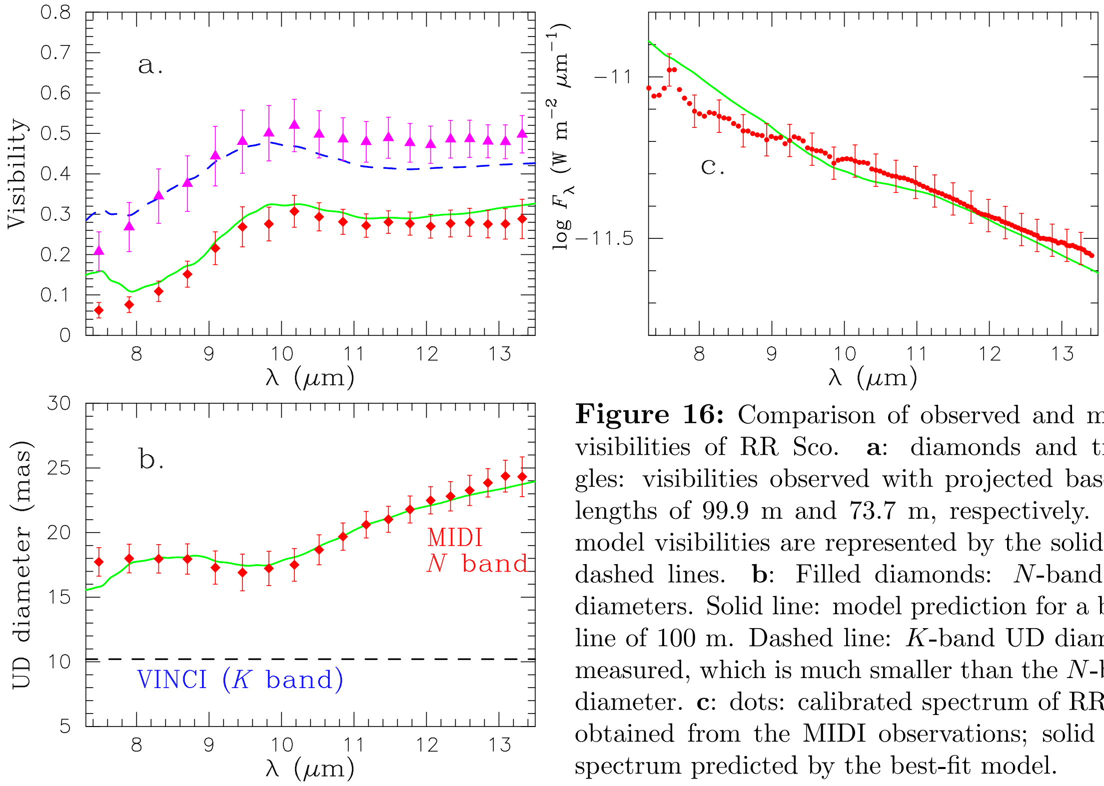

Figure 16: Comparison of observed and model visibilities of RR Sco. **a**: diamonds and triangles: visibilities observed with projected baseline lengths of 99.9 m and 73.7 m, respectively. The model visibilities are represented by the solid and dashed lines. **b**: Filled diamonds: N-band UD diameters. Solid line: model prediction for a baseline of 100 m. Dashed line: K-band UD diameter measured, which is much smaller than the N-band diameter. **c**: dots: calibrated spectrum of RR Sco obtained from the MIDI observations; solid line: spectrum predicted by the best-fit model.

Mid-infrared interferometry of Mira stars provides us with a unique opportunity to study the outer atmosphere and the circumstellar dust shell, where mass outflows are expected to be initiated. We carried out the first mid-infrared spectro-interferometric observations of the Mira variable RR Sco using the MID-infrared Interferometer (MIDI) at the ESO's Very Large Telescope Interferometer (VLTI). The spectro-interferometric capability of MIDI allows us to study the *wavelength dependence* of the object's visibility over the whole N band, between 8 and 13 μm, with $\lambda/\Delta\lambda \approx 30$, as shown in Fig. 16a. The uniform-disk (UD) diameter of RR Sco, which was measured using the unit telescopes UT1 and UT3 with projected baseline lengths of 73–102 m, was found to be 18 mas between 8 and 10 μm, while it gradually increases at wavelengths longer than 10 μm to reach 24 mas at 13 μm (see Fig. 16b). The UD diameter between 8 and 13 μm is significantly larger than the K-band UD diameter of 10.2 ± 0.5 mas measured using VLTI/VINCI with projected baseline lengths of 15–16 m, three weeks after the MIDI observations. Our Monte Carlo radiative transfer modeling (see Fig. 16) shows that optically thick emission from a warm molecular envelope consisting of H_2O and SiO can cause the apparent mid-infrared diameter to be much larger than the continuum diameter. We find that the warm molecular envelope model extending to $\sim$2.3 $R_\star$ with a temperature of $\sim$1400 K and column densities of H_2O and SiO of 3×10^{21} cm^{-2} and 1×10^{20} cm^{-2}, respectively, can reproduce the observed UD diameters between 8 and 10 μm. The observed increase of the UD diameter beyond 10 μm can be explained by an optically thin dust shell consisting of silicate and corundum grains. The inner radius of the optically thin dust shell is derived to be 7–8 $R_\star$ with a temperature of $\sim$700 K, and the optical depth at 10 μm is found to be $\sim$0.025.

→ Ohnaka et al. (2005)

2.4 Near-infrared interferometry of the Mira star *o* Ceti with the VLTI/VINCI instrument and comparison with dynamical model atmospheres

To shed more light on the important question whether Mira stars are fundamental mode or first overtone mode pulsators, we analyzed K band commissioning observations of the Mira star prototype *o* Ceti obtained at the ESO Very Large Telescope Interferometer (VLTI) with the commissioning instrument VINCI and two VLTI siderostats (see Fig. 17).

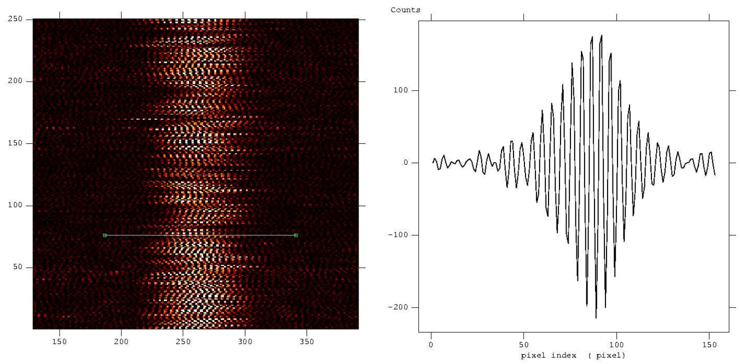

Figure 17: Left: VINCI interferograms of *o* Ceti obtained with a baseline of 16 m. The y-axis shows the interferogram number, and each horizontal line corresponds to an individual interferogram (pseudocolor). **Right**: Single interferogram. The y-axis is given in arbitrary units of relative intensity. In both panels the x-axis gives the pixel number which is a measure of the OPD.

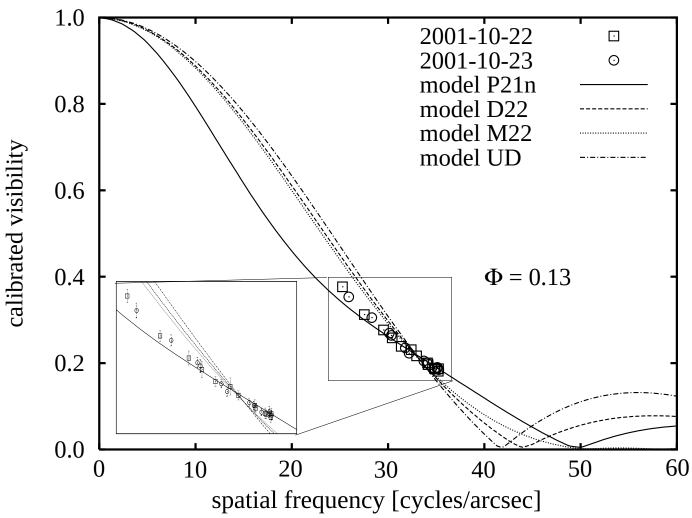

Figure 18: VINCI measurements of the K-band visibility of *o* Ceti at phase $\Phi = 0.13$ obtained in Oct. 2001. The inset shows an enlargement of the relevant spatial frequency range. Here, the error bars are included. The various curves show fits with different Mira star models (Tej et al., A&A, 412, 481 2003, solid lines; Bessell et al., A&A, 307, 481, 1996, dashed lines; Hofmann et al., A&A, 339, 846, 1998, dotted lines), while the dash-dotted line shows the center-to-limb variation corresponding to a uniform-disk model. As the figure reveals, the model P21n from Tej et al. (2003) (solid line) shows best agreement with the measurements.

When comparing the visibilities measured with VINCI to different atmosphere models of Mira stars, we found that the visibilities and apparent sizes measured for *o* Ceti are generally best fitted with the P series fundamental mode pulsator models from Tej et al. (A&A, 412, 481, 2003) and Ireland, Scholz & Wood (MNRAS, 352, 318, 2004) (see Fig. 18). Furthermore, we investigated the variation of the observed visibility function, apparent diameter, and effective temperature with phase. We found that the Rosseland angular diameter of *o* Cet increased from 28.9 ± 0.3 mas ($= 332 \pm 38\ R_\odot$ for an adopted distance of $D = 107 \pm 12$ pc) at variability phase 0.13 to 34.9 ± 0.4 mas ($402 \pm 46\,R_\odot$) at phase 0.4. For the effective temperature we found a decrease from $T_{\rm eff} = 3192 \pm 200$ K at $\Phi = 0.13$ to 2918 ± 183 K at $\Phi = 0.26$.

→ Woodruff et al. (2004)

2.5 Radiative transfer modeling of the warm water vapor envelope around the M supergiants α Ori and α Her

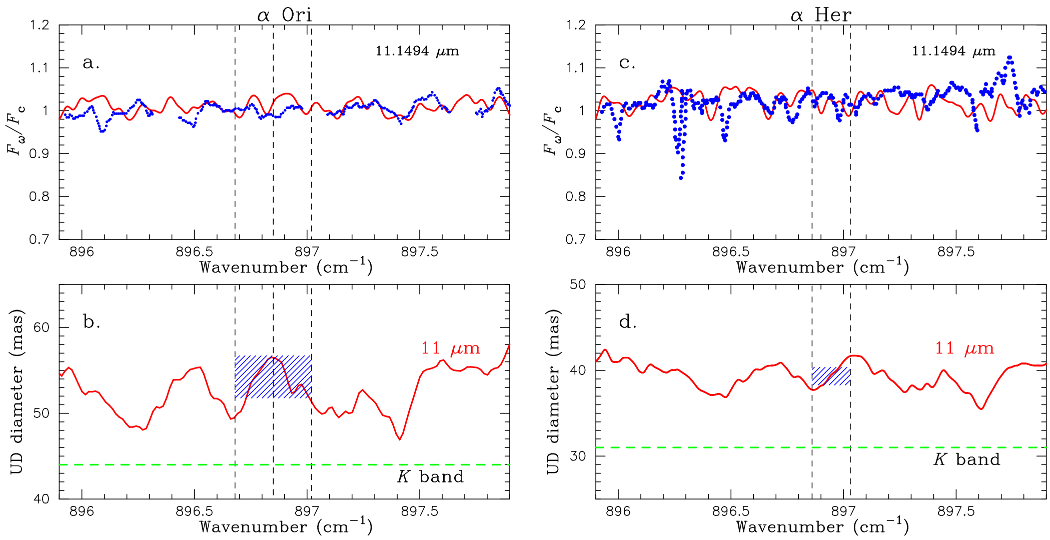

Figure 19: Comparison of the warm water vapor envelope models with the 11 μm interferometric and spectroscopic observations for α Ori and α Her. In panels **a** and **c**, the observed spectra are plotted as dots, while the synthetic spectra are shown as solid lines. In panels **b** and **d**, the observed ranges of the uniform disk (UD) diameters are shown as shaded regions, while the model calculations are plotted as solid lines. The bandpasses used in the 11 μm observations with ISI are marked with the dashed lines. The green dashed lines represent the much smaller K-band UD diameters.

Recent mid-infrared interferometric observations with the Infrared Spatial Interferometer (ISI) by Weiner et al. (ApJ, 589, 976, 2003; not observed by our group) have revealed that the 11 μm angular sizes of the M supergiants α Ori and α Her are ~30% larger than those measured in the K band. This increase of the angular size toward longer wavelengths cannot simply be attributed to a dust shell, as discussed in Weiner et al. (2003). Even more intriguing are the high-resolution 11 μm spectra of α Ori and α Her: there are no salient spectral features within the bandpasses used in the above interferometric observations. Our radiative transfer modeling shows that both the angular diameters and the high-resolution spectra of α Ori and α Her obtained in the 11 μm region can be simultaneously reproduced by a dense, warm water vapor envelope. While prominent absorption due to H_2O can be expected from such a dense, warm water vapor envelope, the absorption lines can be filled in by emission from the extended part of the envelope, making the spectra appear rather featureless, as shown in Figs. 19a and 19c. However, the emission due to H_2O lines from the extended envelope leads to an increase of the apparent size (see Figs. 19b and 19d). The observed angular diameter and the high resolution spectra of α Ori and α Her in the 11 μm region can be best interpreted by a water vapor envelope extending to 1.4 – 1.5 $R_\star$, with a temperature of ~2000 K and a column density of H_2O of the order of 10^{20} cm^{-2}.

→ Ohnaka (2004)

2.6 Modeling of the warm water vapor envelope around Mira variables and a comparison with dynamical model atmospheres

Angular diameter measurements for the Mira variables o Cet, R Leo, and χ Cyg with ISI by Weiner et al. (ApJ, 588, 1064, 2003; not observed by our group) have revealed that the 11 μm

UD diameters are roughly twice as large as those measured in the K band. The observed increase of the angular sizes cannot be solely due to dust emission, as discussed in Weiner et al. (2003). Our radiative transfer modeling shows that these seemingly contradictory observational results can be explained by a simple two-layer model of a dense, warm water vapor envelope (see Fig. 20). The strong absorption due to H_2O expected from such a dense envelope is filled in by emission from the extended part of the envelope, and this results in the high-resolution 11 μm spectra which exhibit only weak, spectral features, masking the spectroscopic evidence of the dense, warm water vapor envelope. On the other hand, the presence of the warm water vapor envelope manifests itself as the larger angular diameters in the 11 μm region compared to those measured in the near-infrared: invisible for spectrometers but not for interferometers. The radii of the hot H_2O layers in the three Mira above variables are derived to be 1.5–1.7 $R_\star$ with temperatures of 1800–2000 K and H_2O column densities of (1–5) $\times$ 10^{21} cm^{-2}, while the radii of the cool H_2O layers are derived to be 2.2–2.5 $R_\star$ with temperatures of 1200–1400 K and H_2O column densities of (1–7) $\times$ 10^{21} cm^{-2}.

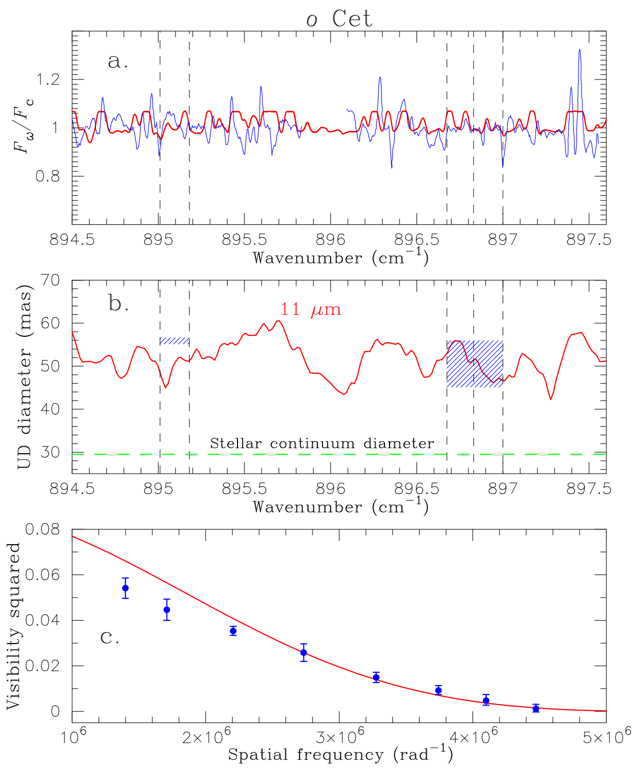

Figure 20: Comparison of our two-layer model for the warm water vapor envelope around o Cet with the 11 μm observations from Weiner et al. (2003). **a:** The spectrum observed at phase 0.36 is plotted as a blue line, while the synthetic spectrum is plotted as a red line. Note that the observed and model spectra appear to be continuum-like in the bandpasses used for the interferometric observations (dashed lines) due to the filling-in effect. **b:** The UD diameters predicted by the model are represented as a solid line, while the observed ranges of the 11 μm UD diameters are shown as the shaded regions. The dashed green line represents the stellar continuum diameter. **c:** Filled circles: squared visibilities measured with ISI at 895.85 cm^{-1}. Solid line: model visibility.

In the next step, we compared the spectra and visibilities predicted by dynamical model atmospheres with self-excited pulsation taken into account (e.g., Hofmann et al., A&A, 339, 846, 1998; Ireland et al., MNRAS, 355, 444, 2004) with the mid-infrared spectroscopic and interferometric observations of o Cet. We found that a fundamental pulsator model with stellar parameters close to those of o Cet can explain the high-resolution spectrum and the UD diameters obtained at 11 μm fairly well. The synthetic spectrum in Fig. 21 shows reasonable agreement with the observed spectrum, although some features in the model spectrum still tend to be somewhat too conspicuous. The predicted UD diameter is also in fair agreement with the ISI observations. This agreement between the model and the observation provides a possible physical explanation for the basic picture of the warm water vapor envelope obtained from the semi-empirical model above.

→ Ohnaka (2004), Ohnaka et al. (2005)

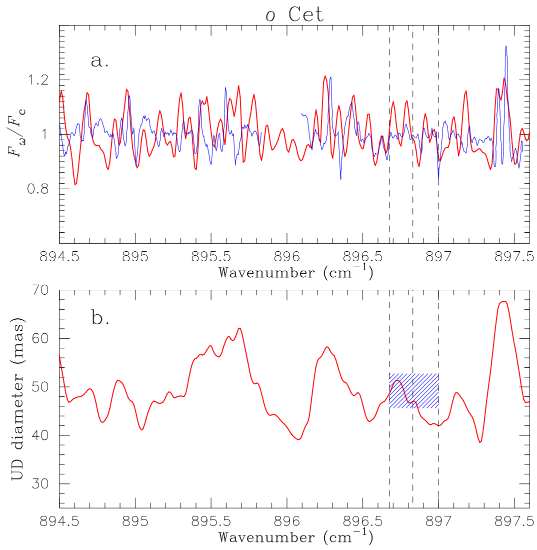

Figure 21: Comparison of a Bessell-Scholz-Wood dynamical model atmosphere in the fundamental pulsation mode with the mid-infrared observations of o Cet. **a:** The spectrum observed at phase 0.36 is plotted as a blue line, while the synthetic spectrum is plotted as a red line. The dashed lines represent the bandpasses used in the ISI interferometric observations. **b:** The UD diameters predicted by the model are represented as a solid line, while the observed ranges of the 11 μm UD diameters are shown as the shaded regions.

2.7 First VLTI/AMBER (2.2 μm) and VLTI/MIDI (8-13 μm) interferometry of the B[e] supergiant CPD$-57°$ 2874

To investigate the questions concerning the origin, geometry, and physical structure of the circumstellar environment of supergiant B[e] stars, it is necessary to combine several observing techniques. We were able to obtain the first direct *multi-wavelength* measurements of a Galactic supergiant B[e] star, namely CPD$-57°$ 2874, an only poorly-studied object so far. Using the VLTI instruments MIDI (mid-IR interferometry with two 8.2 m VLTI telescopes) in Dec 2004 and AMBER (near-IR interferometry with three 8.2 m VLTI telescopes) in Feb 2005, we obtained spectra, visibilities, and closure phases of CPD$-57°$ 2874. We found that the near- and mid-IR interferometric observations of the CSE are well fitted by an elliptical Gaussian model with FWHM diameters varying linearly with wavelength. As shown in Fig. 22, the size, flattening, and orientation of the elliptical Gaussian model significantly change from the K to the N band. For example, the region emitting the mid-IR flux (where the major axis $2a$ is larger than 10 mas = 25 AU at $\lambda \geq 8\mu$m; distance $d = 2.5$ kpc assumed) is more than 2.5 times larger than the one emitting the near-IR continuum flux (where $2a$ is ~ 3.4 mas = 8.5 AU at $\lambda \simeq 2.2\mu$m). The major-axis position angle of the elongated CSE in the mid-IR ($\simeq 144°$) agrees well with previous polarimetric data, suggesting that the hot-dust emission originates in a disk-like structure. In addition, our AMBER observations, which are the first VLTI measurements using three 8.2 m telescopes, reveal a zero closure phase at all wavelengths, indicating that the near-IR emitting regions (continuum and Brγ line) have an approximately centrally-symmetric intensity distribution.

AMBER allowed us to measure, for the first time, both the visibility in the K-band continuum and *in the Brγ emission line* with a spectral resolution of 1500. If we correct the influence of the continuum on the visibility measured in Brγ, we estimate the size (minor $\times$ major axes) of the region responsible for the pure Brγ emission to be $\simeq 2.8\times5.2$ mas (or $\simeq 7.0 \times 13.0$ AU). Thus, the size along the major axis is $\simeq 55\%$ larger than that of the underlying near-IR continuum, but more than 2 times smaller than the mid-IR emitting region ($\lambda \geq 8\mu$m). The near-IR diameters of ~ 10 AU correspond to $\sim 36R_\star$ (assuming $R_\star = 60\,R_\odot$). Therefore, our measurements are compatible with the theoretical CSE diameters computed by Stee & Bittar (A&A, 367, 532, 2001) for a classical Be star.

$\rightarrow$ Domiciano de Souza et al. (2005)

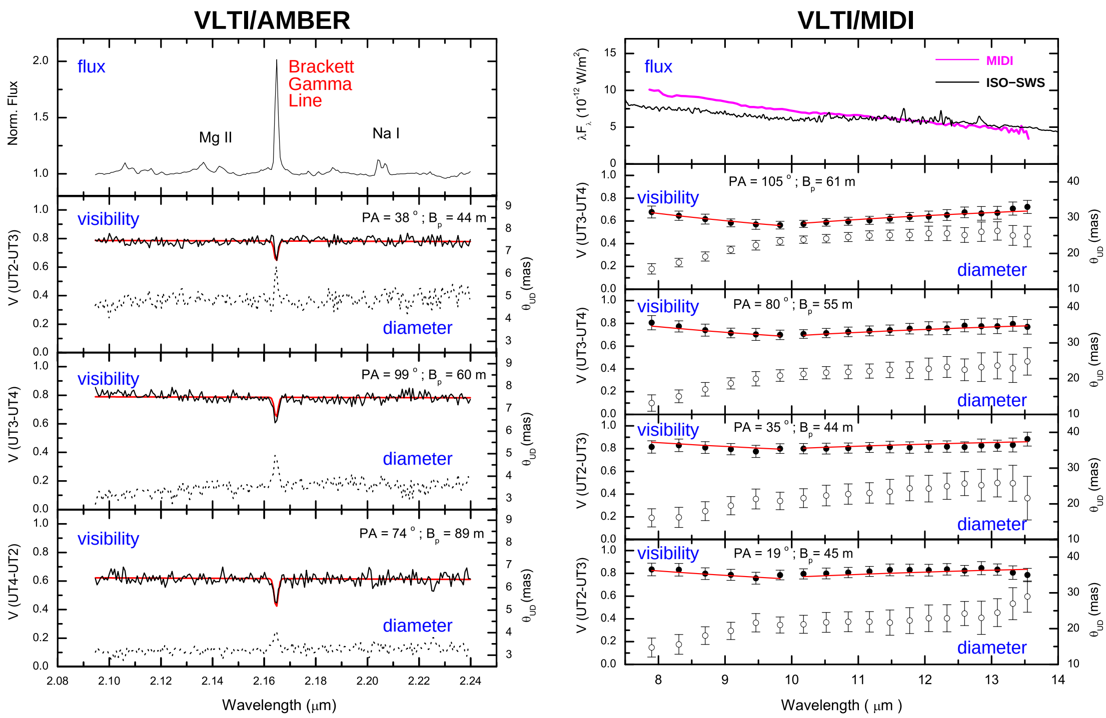

Figure 22: Left: VLTI/AMBER observations of CPD$-57°$ 2874 obtained around Brγ with spectral resolution $R = 1500$. The normalized flux is shown in the top panel and the visibilities V for each baseline are given in the other panels. The errors in V are $\simeq \pm 5\%$. The dotted lines are the uniform disk angular diameters (to be read from the scales on the right axis), computed from V at each λ as a zero-order size estimate. The visibilities obtained from the elliptical Gaussian model fit the observations quite well (smooth solid lines). **Right:** VLTI/MIDI observations of CPD$-57°$ 2874 obtained in the mid-IR with spectral resolution $R = 30$. This figure is organized like the panel on the left, but here V and θ_{UD} are shown as filled and open circles, respectively. The MIDI and ISO-SWS (Sloan et al. ApJS, 147, 379, 2003) spectra (top panel) do not show any clear evidence of a silicate feature around 10μm. The MIDI visibilities are well fitted with an elliptical Gaussian model (solid lines).

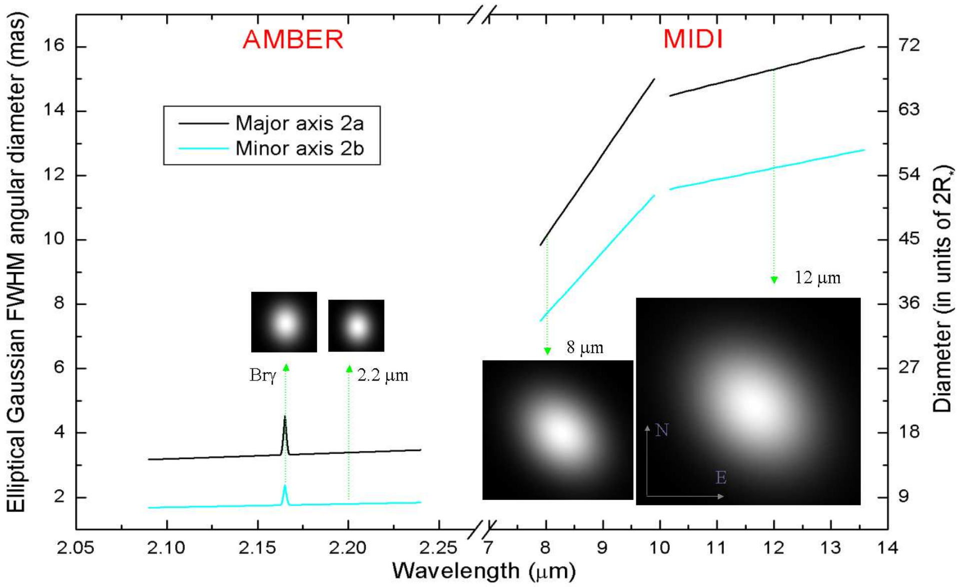

Figure 23: Illustration of the results (size and orientation) derived from the fit of an elliptical Gaussian model to the VLTI/AMBER and VLTI/MIDI visibilities. The scale on the right is given in stellar diameters ($2R_*$). The radius R_* is estimated to be $60 \pm 15\, R_\odot$.

3 Active Galactic Nuclei in the Infrared

The projects described in this section focus on the nucleus of the prototypical Seyfert galaxy NGC 1068, which was the target of the first successful long-baseline interferometric observations of an AGN with ESO's VLTI in both the near- and mid-infrared.

3.1 First near-infrared (2.2 μm) interferometry of NGC 1068 with ESO's Very Large Telescope Interferometer (VLTI)

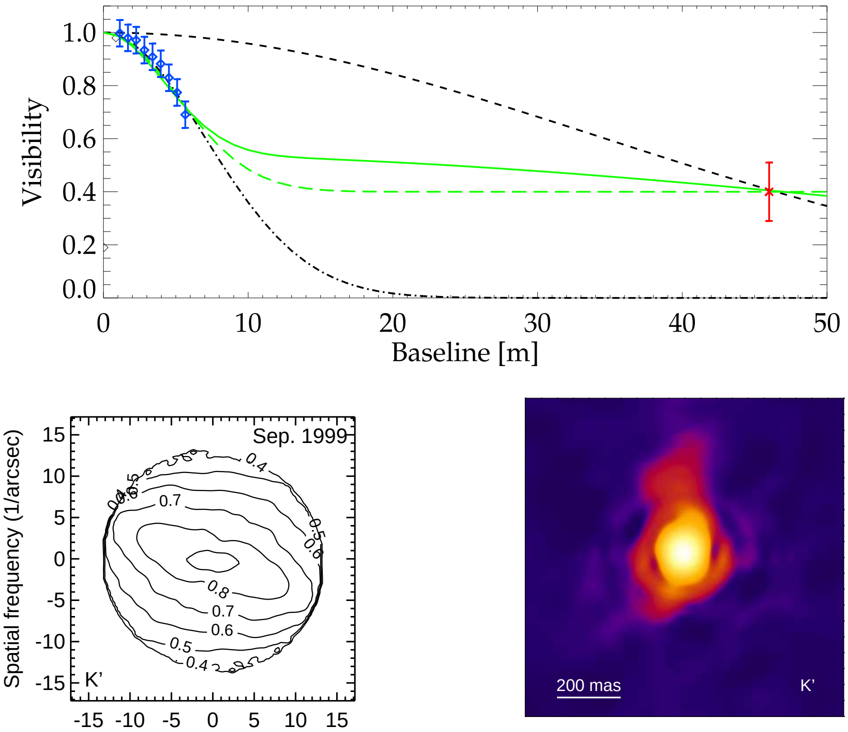

Figure 24: Top: Observed and model K-band visibilities of NGC 1068. The VINCI measurement at a baseline of 46 m and position angle (PA) of 45° is the red visibility point. The visibilities in the baseline range between 0 and 6 m (blue symbols) were obtained from speckle interferometric observations with the SAO 6 m telescope (same PA of 45° as the VINCI observations). The solid green line represents a two-component Gaussian model with 54 % of the total flux from a 3 mas Gaussian (FWHM) and 46 % from a 44 mas Gaussian. The dashed green line represents a model with 40 % of the total flux from a 0.1 mas Gaussian (FWHM) and 60 % from a 36 mas Gaussian. These 2 models illustrate that the size range of the compact component is 0 to 3 mas (the two black lines are 5 and 26 mas Gaussians). **Bottom left:** K-band visibility of NGC 1068 for baselines up to 6 m. The visibilities shown in blue in the top plot are extracted from this 2-D visibility for a baseline orientation of 45°. **Bottom right:** Diffraction-limited image of NGC 1068 reconstructed from the SAO 6 m telescope visibilities (bottom left) and the Fourier phase obtained by bispectrum speckle interferometry.

The radiation from AGN is produced by a central accretion disk and is partly absorbed and scattered in the surrounding dusty torus, as proposed by the Unified Scheme of AGN. The thermal dust emission appears in the near- to far-infrared and shows signatures of the dust content, such as a broad silicate absorption or emission feature. The fuel for AGN activity is assumed to be provided by accretion of interstellar matter from the host galaxy. The dynamics of the cold molecular component of the ISM of the galaxy, in connection with star formation and feedback, channels matter to the nuclear regions where a dusty torus is formed. This torus surrounds the actual nucleus on scales of a few pc.

Using two 8.2 m telescopes of the VLTI and the beam combiner instrument VINCI, we obtained the first near-infrared K-band visibility of NGC 1068 measured with a long baseline. At a projected baseline length of 46 m and position angle of 45°, the observed squared visibility amplitude is 0.16 ± 0.04. Taking into account the K-band speckle interferometry observations (see Fig. 24), the observations suggest a multi-component model for the intensity distribution, where one part of the flux originates from scales clearly smaller than 3 mas (0.2 pc) and another part comes from larger scales. Thus, it is the smallest object ever observed in the torus region of NGC 1068. The K-band emission from this small (≤ 3 mas) component might arise from substructure of the dusty nuclear torus or directly from the central accretion flow viewed through only moderate extinction. Both possibilities are in line with the concept of a clumpy torus (see. Sec. 3.4), where clouds are randomly distributed.

→ Weigelt et al. (2004), Wittkowski et al. (2004)

3.2 First mid-infrared $8 - 13\,\mu$m MIDI/VLTI observations of the dusty torus in the nucleus of NGC 1068

NGC 1068 was the first extragalactic object ever observed using mid-infrared interferometry. The observations were carried out with the beam combiner instrument MIDI and two 8.2 m telescopes of ESO's VLT Interferometer in the $8 - 13\,\mu$m wavelength range. The extended structure and the orientation of the spectroscopic MIDI slit (white box) in Nov. 2003 with a 42 m baseline is shown in Fig. 25. The 2 northern arms are aligned with both the radio jet and the ionization cone. The total and correlated fluxes from two observations are given in Fig. 25 and show that the nucleus is resolved in the mid-infrared (with a resolution of ~ 26 mas for a baseline of 42 m and ~ 13 mas for a 78 m baseline).

The data can be interpreted in terms of a simple two-component model consisting of warm (320 K) dust in a 2.1×3.4 pc elliptical structure surrounding a smaller hot component. The major axis of this elongated 320 K structure is approximately perpendicular to the jet axis. The interferometric measurement constrains the size of the hot component to 0.7 ± 0.2 pc along and ≤ 1 pc perpendicular to the jet axis and requires a temperature above 800 K. The spectra in Fig. 25 show a broad silicate absorption feature near $\sim 10\,\mu$m. The absorption is more pronounced in the correlated fluxes, which indicates that the hot component is embedded within the extended component. Interestingly the minimum shifts to longer wavelength with increasing baseline and the feature appears asymmetric with a steeper slope at the short wavelength side. The two-component model explains this as a combination of non-standard, calcium aluminium silicate dust and the smaller size of the hot component, which leads to larger correlated fluxes at shorter wavelength.

The observed 2.1×3.4 pc structure is interpreted as the inner hot wall of a geometrically thick dust torus. Radiative transfer calculations of the torus with homogeneous dust distributions apparently fail to reproduce the size and optical depth of this structure. This suggests that the dust in the torus is arranged in clouds. This finding is in agreement with the inferred clumpiness from the K-band VINCI/VLTI observations (Sec. 3.1). It is thus necessary to include the clumpiness in radiative transfer calculations. A more detailed modeling of the inhomogeneous structure of the proposed nuclear torus is the subject of the theoretical investigations described below (Sec. 3.4).

→ Jaffe et al. (2004)

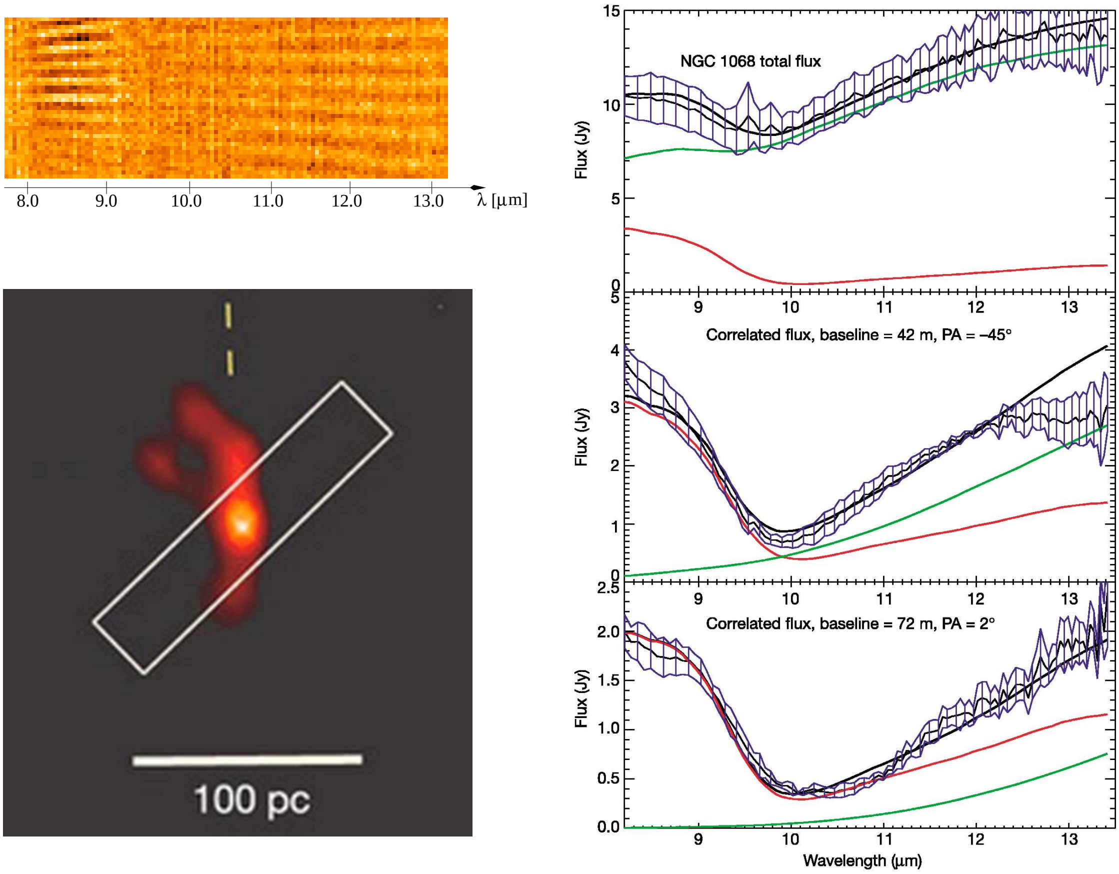

Figure 25: Mid-infrared long-baseline interferometry of NGC 1068 using the MIDI instrument of ESO's VLT interferometer. **Top left:** One of the N-band interferograms of NGC 1068 obtained with MIDI. **Bottom left:** Single-telescope acquisition image of NGC 1068 taken with a 8.7 μm filter. **Right panel:** The plots show the observed fluxes as a function of wavelength, where the blue-lined areas show their r.m.s. scatter in independent observations. The thick smooth black line represents a simple model as the sum of the red and green lines, which show the contribution of a hot and warm component, respectively. **Top right:** The single-telescope, non-interferometric MIDI flux-density spectrum. The absorption dip near 10 μm is primarily caused by astronomically common silicate dust. **Middle right:** The two-telescope interferometric spectrum (correlated flux) from November 2003 with a projected baseline of 42 m oriented at position angle 45°. **Bottom right:** The interferometric spectrum from June 2003 with a projected baseline of 78 m at position angle 2°.

3.3 Theoretical studies of accretion from galactic gas disks to the circum-nuclear torus of AGN

Supernova-driven turbulence in the clumpy gas disk of galaxies. Studies of the cold, molecular phase of the ISM in galactic disks are essential for an understanding of the evolution of spiral galaxies and the related fueling of AGNs. For this, we developed a simplified analytical model of a turbulent and clumpy gas disk in spiral galaxies. In this model, turbulence in the ISM is maintained by the mechanical energy input due to supernovae. Properties of the molecular disk, such as global filling factors, molecular fractions, and star formation rates, are found to be determined by the mass accretion rate $\dot{M}$ within the disk, the time constant of molecule formation α, and the local angular velocity of the disk. Two different cases for the gravitational potential have been investigated: a dominating stellar disk and a vertically self-gravitating gas disk. The driving length scale of the turbulence is determined by the supernova energy input. The energy is then cascaded to smaller scales

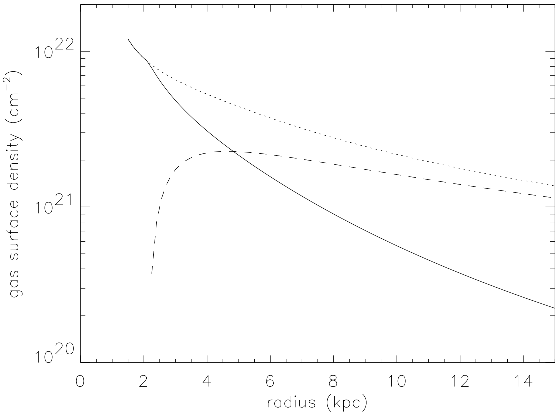

Figure 26: Radial profiles of the total (dotted line), molecular (solid line), and atomic (dashed line) gas surface density for a supernova-driven model of the cold phase of the ISM in normal spiral galaxies.

by the turbulence, where it is dissipated. In an alternative approach, the driving length scale is directly determined by the size of supernova remnants. Both models have been applied to the Galaxy and are able to reproduce integrated and local gas properties. The radial density profiles of the molecular and atomic gas phases, as derived from the model, are shown in Fig. 26. The resulting atomic gas density shows a hole with a radius of 2 kpc in the center. We find that the cold gas disk is marginally unstable (Toomre-$Q \sim 1$) and infer a mass accretion rate of $\dot{M} \sim 0.05 - 0.1\,M_\odot\,\mathrm{yr}^{-1}$ for the Galaxy. This implies that the mass accretion rate must drop dramatically from the disk of the galaxy to the supermassive black hole Sgr A*, since the luminosity of Sgr A* requires $\dot{M} \leq 10^{-6}\,M_\odot\,\mathrm{yr}^{-1}$. The accretion process is therefore non-stationary and/or most of the matter channeled to the center is lost in winds or consumed in star formation. This is supported by the state of the circumnuclear disk in the center of the Galaxy on scales of a few pc, described below, which demands an intermediate accretion rate.

From the Circumnuclear Disk in the Galactic Center to thick, obscuring tori of AGNs. By comparing three different models of a clumpy gas disk, we show that both the circumnuclear disk (CND) in the galactic center of our Galaxy and a putative, geometrically thick, obscuring torus around an AGN can be explained by a collisional model. The basic constituents are quasi-stable, self-gravitating, molecular, and dusty clouds orbiting in the region of the torus. The clouds gain kinetic energy by mass inflow which is subsequently dissipated in cloud collisions. The collisions give rise to an effective viscosity in a gas dynamical picture, which leads to angular momentum transport and mass inflow. It is found that the CND and the torus share the same gas physics in our description; the mass of individual clouds is approximately $20 - 50\,M_\odot$ and their density is close to the limit of disruption by tidal shear. We show that the differences between a transparent CND and an obscuring torus are the gas mass and velocity dispersion of the clouds. A change in gas supply and the dissipation of kinetic energy can turn a torus into a CND-like structure and vice versa. The existence of a massive torus will naturally lead to sufficiently high mass accretion rates to feed a luminous AGN. In a detailed investigation of stationary models for obscuring dusty tori around AGN, the vertical and radial structures of the torus are derived from a dynamical approach for the evolution of an ensemble of clouds. We constructed an exact solution for the quasi-isothermal vertical cloud distribution, which is valid for an arbitrary thickness of the torus with a wide funnel along the symmetry axis. The radial structure of the accretion flow is a consequence of cloud-cloud collisions. Accretion in the combined gravitational potential of a central black hole and a nuclear stellar cluster generates free energy, which is dissipated in the collisions, and thus maintains the thickness of the torus. A meridional cut through the

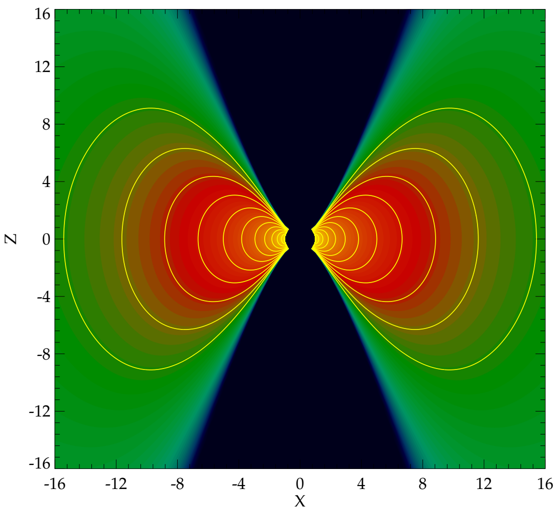

Figure 27: Mass density contours in the meridional plane of our torus model. Contour levels decrease by a factor of 2 from the density peak. The vertical scale-height and the mean free path between clouds are assumed to be equal. The spatial scale is in units of the dust sublimation radius, which is about 1 pc for the case of NGC 1068.

average mass density distribution of the obtained torus model is shown in Fig. 27. The mass density distribution determines the probability of finding clouds at all positions in the torus. This allows us to derive the mean optical depth of our torus model. We find that obscuration of the nucleus, as required by Unified Schemes of AGN, is achieved for large mass accretion rates above the Eddington limit of the central black hole. The mean number of clouds in the midplane of the torus along a line of sight to the center is about 10. The implications for the appearance of such a clumpy torus in radiative transfer calculations are discussed in Sec. 3.4.

→ Beckert & Duschl (2004), Vollmer & Beckert (2003), Vollmer et al. (2004)

3.4 Radiative transfer modeling of the infrared emission from clumpy AGN tori: First clumpy torus models of NGC 1068

The Unified Scheme of AGN postulates that the actual nucleus is surrounded by a dusty torus which is held responsible for aspect angle dependent obscuration. This scenario can explain the differences between type 1 and type 2 AGNs and predicts a silicate feature at about 10 μm, either in emission or absorption. Recent bispectrum speckle interferometry observations of the torus region in NGC 1068 with high spatial resolution in the H- and K-band and long-baseline interferometry using the VLTI are described in Sec. 3.1 and 3.2. They allow, for the first time, a detailed comparison of torus models with measured SEDs, images, and visibilities. We have combined our newly developed model of a clumpy torus, presented in Sec. 3.3, with a statistical approach for radiative transfer in a clumpy medium (Nenkova et al., ApJ, 570, L9, 2002). In the first step, statistical averages for the emitted radiation from a distribution of clouds in the torus are calculated. The method makes use of a database of cloud models generated from radiative transfer calculations of rotated 1-D slabs, which were averaged to simulate dusty spheres. In the second step, the cloud models serve as building blocks for the torus model. The model assumes a dust composition of silicates and graphite grains typical for the ISM of our Galaxy.

A comparison of these model calculations with observations of NGC 1068 is shown in Fig. 28. The suggested model requires a mass accretion rate of $2.5\,M_\odot\,\mathrm{yr}^{-1}$ in the torus region. The inferred AGN luminosity is $L = 2.2 \times 10^{45}\,\mathrm{erg\,s}^{-1}$, which corresponds to about the Eddington luminosity of a $10^7\,M_\odot$ black hole. The modeled SED shows satisfactory agreement with photometric observations. The mid-infrared spectrum measured with MIDI indicates a non-standard dust composition in the torus, which we hold responsible for the

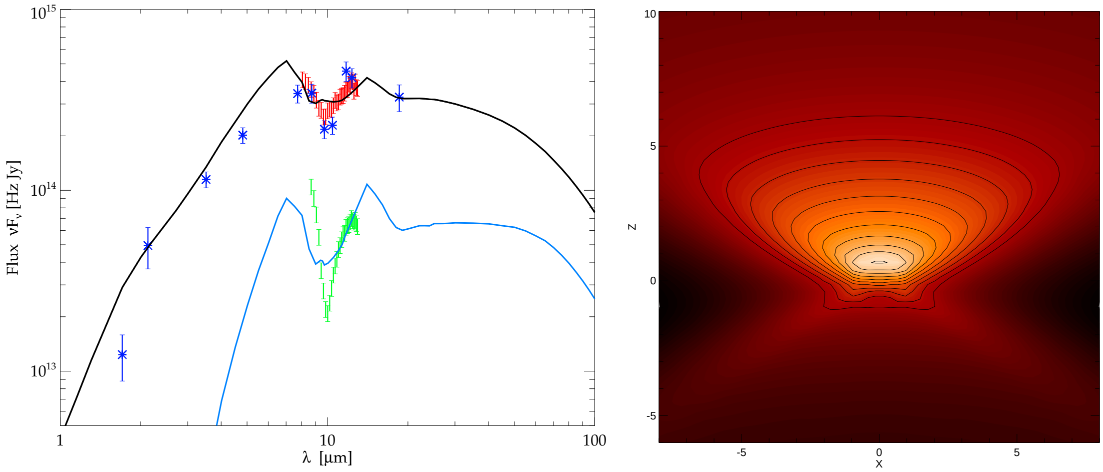

Figure 28: Left: Comparison of observed infrared fluxes from the nucleus of NGC 1068 with the SED of a clumpy torus model. The inclination of the torus axis is 75° (close to edge-on). The red bars show the total flux in the range of 8 to 13 μm measured with the MIDI/VLTI instrument. The green bars give the correlated flux for the 42 m projected baseline at a PA of 45°, as described in Sec. 3.2. Individual photometric measurements between 1.7 and 18 μm are represented by the blue symbols. The black line is the total SED derived from our model, while the blue line shows the correlated flux of our model for baseline length and PA 45° of the MIDI measurements. **Right:** Simulated K-band ($\lambda = 2.2\,\mu$m) surface brightness distribution of our dusty and clumpy torus model for the same model parameters as used for the calculation of the SED. The spatial scale is in units of the dust sublimation radius. Contour levels decrease by a factor of 2 from the peak.

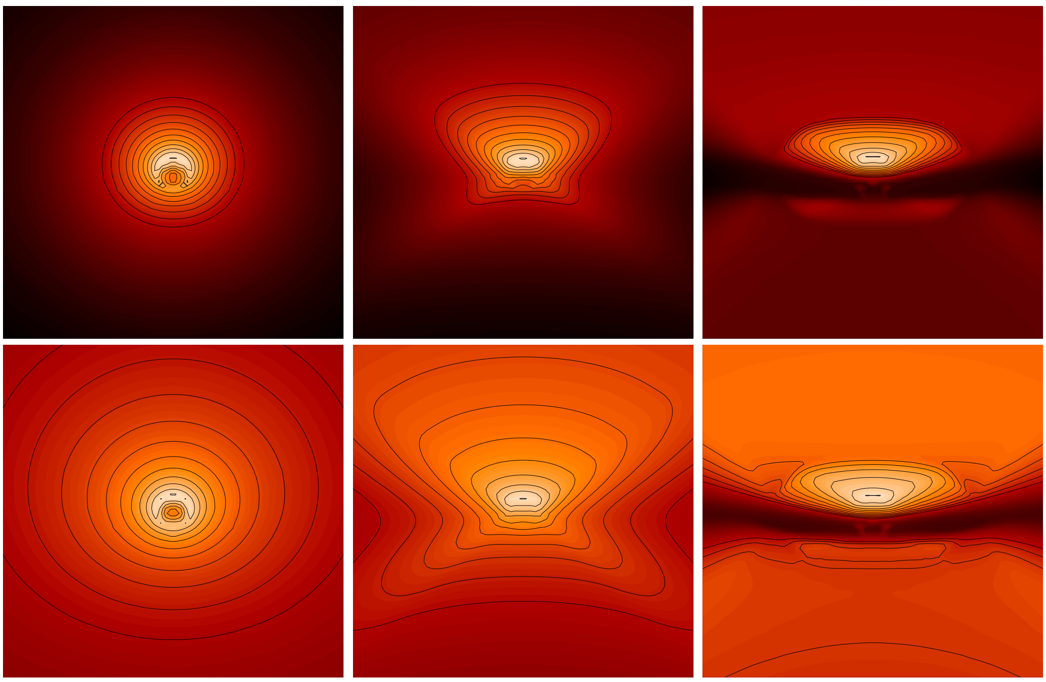

Figure 29: Near- and mid-infrared model images of the surface brightness distribution. A region with a size of 10×10 sublimation radii centered on the black hole is shown. The upper panel shows K-band ($\lambda = 2.2\,\mu$m) images for inclinations $i = 60°, 20°$, and $10°$ (from left to right). The lower panel shows N-band ($\lambda = 11\,\mu$m) images for the same inclinations. The contour levels decrease by a factor of 2 from the peak in each image.

differences in the shape of the silicate absorption feature, both in the total and the correlated flux. The resulting K-band image for the preferred inclination of $75°$ is also shown in Fig. 28. It shows that the long axis of the core seen in H- and K- band speckle observations (core size (FWHM) $\sim 18 \times 39$ mas or 1.3×2.8 pc) corresponds to about four times the sublimation radius. A sample of model images for the same parameter set but different inclinations at near- and mid-infrared wavelengths is shown in Fig. 29. While the core radius does not change much with wavelength the extended emission is larger in the mid-infrared, in agreement with the observations.

→ Beckert (2005)

People involved: T. Beckert, A. Domiziano de Souza, T. Driebe, M. Eberhardt, K.-H. Hofmann, S. Hönig, S. Kraus, R. Lachaume, K. Murakawa, K. Ohnaka, Th. Preibisch, D. Riechers, A. Rosen, D. Schertl, K. Smith, G. Weigelt, C.H. Woodruff.

Collaborations:

K. Agabi(Univ. Nice), D. Apai (Steward Observatory, Univ. of Arizona), P. Antonelli (Observatoire de la Côte d'Azur, Grasse), E. Aristidi (Univ. Nice), C. Baffa (Osservatorio Astrofisico di Arcetri, Florence), I. I. Balega, Y. Y. Balega (Special Astrophysical Observatory, Russia), M. Benisty (Univ. Joseph Fourier, Grenoble), J.-P. Berger (Univ. Joseph Fourier, Grenoble), H. Beuther (MPIA Heidelberg), A.G.A. Brown (Sterrewacht Leiden), W.J. de Witt (Univ. Joseph Fourier, Grenoble), O. Chesneau (Observatoire de la Côte d'Azur, Grasse), A. Chelli (Univ. Joseph Fourier, Grenoble), W.J. Duschl (Univ. Heidelberg, Steward), M. Duget (Observatoire de la Côte d'Azur, Grasse), G. Duvert (Univ. Joseph Fourier, Grenoble), M. Elitzur (Univ. of Kentucky), P. Feautrier (Univ. Joseph Fourier, Grenoble), E. Feigelson (Pennsylvania State Univ., USA), R. Foy (Centre de Recherche Astronomique de Lyon), D. Fraix-Burnet (Univ. Joseph Fourier, Grenoble), L. Glück (Univ. Joseph Fourier, Grenoble), G.H. Herbig (Univ. of Hawaii), A. Isella (Osservatorio Astrofisico di Arcetri, Florence), M. Kiekebusch (ESO, Paranal, Chile), S. Lagarde (Observatoire de la Côte d'Azur, Grasse), E. Le Coarer (Univ. Joseph Fourier, Grenoble), Ch. Leinert (MPIA Heidelberg), F. Lisi (Osservatorio Astrofisico di Arcetri, Florence), B. Lopez (Observatoire de la Côte d'Azur, Grasse), F. Malbet (Univ. Joseph Fourier, Grenoble), A. Marconi (Osservatorio Astrofisico di Arcetri, Florence), P. Mathias (Observatoire de la Côte d'Azur, Grasse), A. Meilland (Observatoire de la Côte d'Azur, Grasse), S. Mensh'chikov (Inst. for Comput. Astrophysics, Halifax), M. Meyer (Steward Observatory, Univ. of Arizona), F. Millour (Univ. Nice), J.-L. Monin (Univ. Joseph Fourier, Grenoble), D. Mourard (Observatoire de la Côte d'Azur, Grasse), A. Natta (Osservatorio Astrofisico di Arcetri, Florence), A.S. Miroshnichenko (University of Toledo, USA), I. Pascucci (Steward Observatory, Univ. of Arizona), K. Perraut (Univ. Joseph Fourier, Grenoble), C. Perrier (Univ. Joseph Fourier, Grenoble), R. Petrov (Univ. Nice), A.M. Prieto (MPIA, Heidelberg), P. Puget (Univ. Joseph Fourier, Grenoble), Y. Rabbia (Observatoire de la Côte d'Azur, Grasse), A. Richichi (ESO, Garching), S. Robbe-Dubois (Univ. Nice), PṠalinari (Osservatorio Astrofisico di Arcetri, Florence), M. Schöller (ESO, Paranal, Chile), M. Scholz (Univ. Heidelberg, Univ. Sydney), M.D. Smith (Armagh Observatory, Northern Ireland), P. Stee (Observatoire de la Côte d'Azur, Grasse), E. Tatulli (Univ. Joseph Fourier, Grenoble), L. Testi (Osservatorio Astrofisico di Arcetri, Florence), P. Tuthill (Univ. Sydney), R. van Boekel (MPIA Heidelberg), M. Vannier (Univ. Nice), B. Vollmer (Univ. Strasbourg), M. Wittkowski (ESO, Garching), P.R. Wood (Australian Nat. Univ., Canberra), E. Young (Steward Observatory, Univ. of Arizona), F. Yuan (Academy of Science, Shanghai), H. Zinnecker (Astrophysikalisches Institut Potsdam), G. Zins (Univ. Joseph Fourier, Grenoble).

4 Very high energy particles in the universe and the activity of black holes

The theory group has contributed to the physics of: 1) High Energy Particle Physics in the Galaxy: The Origin of Galactic Cosmic Rays. 2) The Highest Energy Cosmic Rays: From Nearby Black Holes, Active and In-active. 3) The Origin and Physics of Cosmic Magnetic Fields. 4) Very High Energy Cosmic Rays: The Distant Black Holes - Physics beyond the Standard Model? 5) Dark Matter: A Solution?

4.1 High Energy Particle Physics in the Galaxy: The Origin of Galactic Cosmic Rays

Galactic cosmic ray particles extend in energy to about $3\ 10^{18}$ eV, so far beyond any accelerator on Earth, in existence or even planned. Their sources must be among the known objects in the Galaxy, stars and their explosions, gamma ray bursts, the interstellar medium, as well as the final stages of stars, white dwarfs, neutron stars and stellar black holes. Or there could be a connection to dark matter, to be discussed below. The emphasis of our work here was to connect the origin and interactions of the galactic cosmic rays to the physics of the stars, that explode, and their immediate environment. This approach has proven successful.

We had proposed a wind-supernova model to account for the cosmic rays at all energies, and we have been testing and developing this theory. Since the EGRET satellite data demonstrated that there is an unexplained excess in the γ-ray spectrum of the inner Galaxy, we have applied the original model to describe the cosmic ray interactions. We find, that we have to differentiate the sources of cosmic rays into three groups:

Stellar explosions from stars of a zero age main sequence (ZAMS) mass between 8 and about 15 solar masses. These stars explode into the interstellar medium, and accelerate cosmic rays in their shocks, with a predicted spectrum of $E^{-2.42\pm0.04}$, where E is the cosmic ray particle energy, but dominate mostly for protons as well as electrons, and not for any other element in the cosmic ray abundances.

Stellar explosions from stars of a ZAMS mass between 15 and about 25 solar masses. Such stars explode into their own wind, accelerate cosmic rays in their shocks running through the wind, but that wind is not so powerful, and does not extend very far. Wind supernovae produce a spectrum of $E^{-2.35\pm0.02}$. These stars are known near the end of their life as Red Supergiants stars (RSG). When the cosmic ray laden shock hits the shell, the shell is disrupted convectively, and so the resulting gamma ray spectrum corresponds to the injection spectrum; this dominates the EGRET spectrum.

Stellar explosions from stars of a ZAMS mass above about 25 solar masses. Such stars explode into their own wind, but in this case the wind is very powerful, and extends far. In this case the cosmic rays are accelerated in the supernova shock running through the heavily enriched wind. These stars are known near the end of their lifetime as Wolf Rayet (WR) stars, and provide most of the heavy elements in cosmic rays. When the cosmic ray laden shock hits the shell, the shell is disrupted diffusively, and so the resulting gamma ray spectrum corresponds to the injection spectrum steepened by $E^{-5/9}$; this dominates the γ-ray spectrum only at energies above 10^{15} eV (=PeV), and is a testable prediction in the future, since this gamma ray spectrum extends close to EeV energies. For the spectrum beyond the knee, the bend in the overall cosmic ray spectrum near $3\ 10^{15}$ eV, we predicted $E^{-3.14\pm0.07}$. The interaction in the shell and the immediate environment also produces the well-known

Boron and other light element abundances.

Our model taking all these star properties into account can explain the data, see the figure; it shows the measurements of EGRET, and the upper limits of the Whipple telescope, KASKADE, CASA-MIA; it matches the data from MILAGRO and HESS.

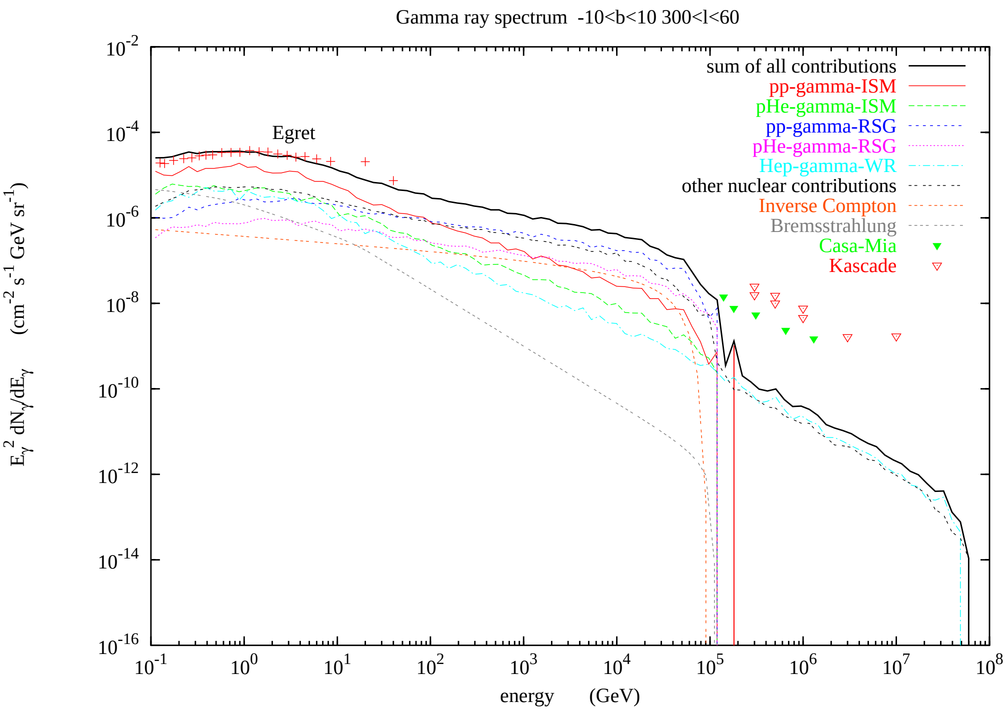

Figure 30: The fit of our wind-supernova model based on different stellar types and their explosions to the EGRET data across PeV through EeV energies. We differentiate between the various source contributions, and predict the γ-ray spectrum shown here for the inner Galaxy. In the graph the different contributions are shifted by an arbitrary amount to facilitate reading. The model also matches all other observational constraints, upper limits are inverted triangles from the Whipple telescope, KASKADE, and CASA-MIA; it matches the data from MILAGRO and HESS.

The argument that most interaction of cosmic rays happens near the source has found some additional recent successes:

Isotopic precise abundances have reminded us of Wolf Rayet stars for some time. Integrating the abundance contributions from the various stars, using a proper initial mass function, reproduces the cosmic ray abundances. It also leads to the prediction that the very massive stars all explode with 10^{52} erg, so matching a well known argument on hypernovae, and gamma ray bursts.

Exploring the physics of the knee, the bend between two powerlaws in the cosmic ray spectrum near 3 10^{15} eV, has led to a confirmation of the magneto-rotational mechanism for the Supernova mechanism, proposed as a concept by Kardashev (Astron. Zh., 41, 807, 1964) and specific proposal by Bisnovatyi-Kogan (Astron. Zh, 47, 813, 1970). This mechanism naturally includes a mechanism for jet-supernovae, and Gamma Ray Bursts.

Spallation at a young age of the Galaxy: There is sofar no other way to explain the very old star abundances in the light elements Li, Be, B (Reeves, astro-ph/0509380, 2005). Already at a young age, spallation near the source implies secondary nuclei in a locally heavily enriched environment, the winds of very massive stars just before they blow up.

Anti-protons and positrons: the standard cosmic ray model cannot fit the γ-ray spectrum, nor the positron and anti-proton spectrum; the wind-supernova model can.

The success of the wind-supernova model to provide a fully consistent explanation for these data, all obtained many years after the quantitative model was proposed, lead to the hope that perhaps we are closing in over the next few years on a physical understanding of the origin of Galactic cosmic rays.

Therefore one may expect that the the most exciting laboratories for the acceleration of heavy nuclei are the explosions of Wolf Rayet stars, and Gamma Ray Bursts.

→ Abraham et al. (2004), Biermann et al. (2004), Biermann (2005a), Biermann (2005b), Casanova et al. (2004), Lämmerzahl et al. (2004), Meli & Biermann (2004), Quenby & Meli (2004), Tudose & Biermann (2004)

4.2 The Highest Energy Cosmic Rays: From Nearby Black Holes, Active and In-active

The highest energy cosmic ray particles allow to push our understanding of the structure of matter to its limit, but require an understanding of their possible sources, and transport as well as interaction modes. There are basically two classes of sources, within about 50 Mpc distance from us, and at larger distances; this distance is a critical milestone since high energy protons and neutrons suffer from interactions in the microwave background, and cannot come to us from larger distances. So, if the sources are nearby, then we can possibly identify the cosmic accelerators, and do our "experiments" with them, or if they are distant, they are the sign of physics beyond the Standard Model. We explore both options, see below.

From our earlier work on active galactic nuclei we have estimated the contribution of cosmic rays from any compact radio source associated with a black hole. The theory allows us to estimate the maximum particle energy, and also the maximum contributed flux. We use here the well-tested concept of shock acceleration in the compact relativistic jet, arising from the inner ring of the accretion disk, very close to a rapidly spinning black hole. We have been able to show how the spin down of a black hole combines with accretion to provide an apparent efficiency of conversion of accretion energy into jet power at a level exceeding 100 percent.

The observed nearby black holes

We use the formulae derived by us earlier to use the data on compact radio emission from near to any black hole to estimate maximum particle energy and expected CR flux.

We have determined the expected high energy cosmic ray flux from all nearby black holes, known to be active.

The conclusion from these calculations is, that at the highest energy only the radio galaxy M87 contributes, as has been claimed for many years, see the figure. Second, at lower energy, Cen A may indeed take over as the second most important source, again as expected for some time. So radiogalaxies are cosmic accelerators then, and prime laboratories for very high energy physics.

→ Biermann et al. (2005), Biermann & Medina Tanco (2003), Falcke et al. (2005)

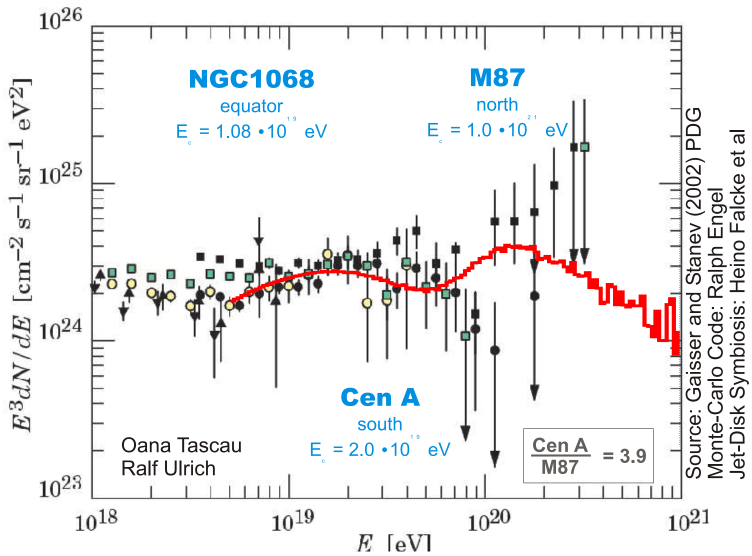

Figure 31: Our predicted spectrum of the cosmic ray contributions at high energy from the cosmologically nearby active black holes. Only the nearby radio galaxies M87 and Cen A contribute significantly. The data shown are from the various ultra high energy cosmic ray arrays, such as AGASA, HiRes, and earlier experiments, taken from the PDG review by Gaisser & Stanev. The AGASA data suggest an upturn of the spectrum, while the HiRes data suggest a downturn at high energy.

4.3 The Origin and Physics of Cosmic Magnetic Fields

The role of the magnetic field is still a gaping hole in our physical understanding, both in its importance for the transport and acceleration of cosmic rays, as in our understanding of the origin of magnetic fields.

The old approach was to use the battery mechanism to create weak fields in the galaxy, and then strengthen them with a dynamo process, over long times. The dynamo process consists of the rising of a magnetic loop, twisting it, and folding it back down; this is a slow diffusive process. A cosmic ray driven dynamo operates on the rotation time scale at best. Any regular magnetic field in the ISM is turned chaotic on the ISM time scale of 3 107 years, which is much less than the rotation period. Therefore the destruction time scale of the magnetic field order is a small fraction of the rotation time scale, and so we do require a mechanism which is faster than a single rotation period or any even slower processes. Using Maxwell's laws to infer the required conditions leads us to the speculation, that perhaps large scale shocks provide two dimensional electric currents, vertical sheet currents; if such currents were to exist, then a lowest order constant large scale magnetic field could be provided.

Matching the HESS and other data for young supernova remnants implies that the magnetic field is considerably enhanced in shocks, perhaps by local instabilities, or perhaps by electric current systems. This may imply the same requirement as the symmetry argument from the overall magnetic field in galaxies.

We calculate the orbits of protons in a Galactic halo-wind, described by a Parker topology magnetic field with a k^{-2} saw-tooth turbulence spectrum (k is the wavenumber); a typical result is shown. We developed advanced wind models, and treated also the propagation at the energy transition between Galactic and extragalactic cosmic rays.

The pattern of the arriving cosmic rays across the sky will be a key test to differentiate between the source model of nearby activity, and very distant activity, see the figure: If there are just a few nearby sources, the sky will be very patchy at high energy, but if distant sources dominate, in whatever detailed mechanism, the sky will remain smooth.

→ Biermann & Kronberg (2004), Biermann & Galea (2003)

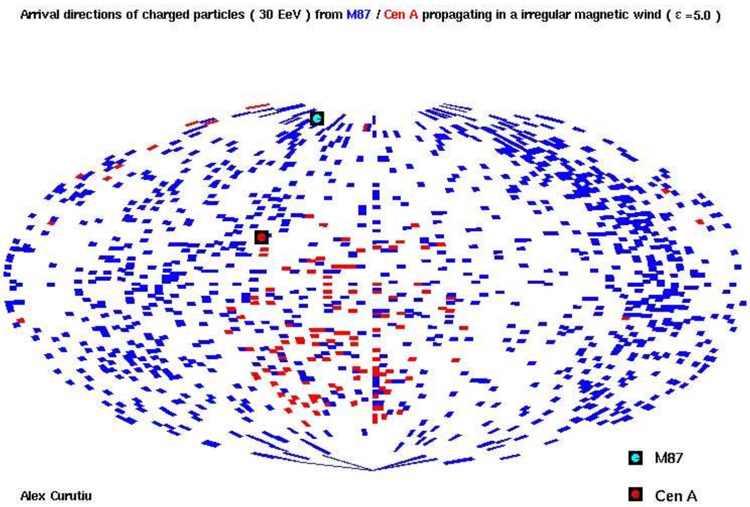

Figure 32: We show the arrival directions of high energy cosmic rays in our model for the Galactic halo wind with maximal turbulence. We follow the orbits of energetic particles from only two sources, the radio galaxies M87 and Cen A. The magnetic field irregularities isotropize all arrival directions completely at the energy chosen here, $3\ 10^{19}$ eV, at maximal turbulence. For the case of weaker turbulence or much higher particle energy isotropy cannot be maintained, so this model has predictive power. A typical result is shown for weak irregularities, or, equivalently, for very high particle energy.

4.4 Very High Energy Cosmic Rays: The Distant Black Holes - Physics beyond the Standard Model?

The apparent contradiction between the HiRes and the AGASA results, one showing an apparent continuation of a powerlaw spectrum to high energy (AGASA), while the other seems to show the expected drop-off with higher energy (HiRes), has not yet been resolved by AUGER. It is completely unclear at present, whether the discrepancy is solely in the data analysis, and also which, if either one of these results is a better match for reality. Therefore we estimate any plausible association in direction between reasonable samples of active sources, but now cosmologically distant sources, a tell tale sign of physics beyond the Standard Model, if an association could be found.

The statistics of positional coincidences demonstrate that for a radio sample coupled with a far-infrared selection the probability that the directional coincidence is random is very small; however since this is a posteriori statistics this is not a claim that can be sustained. Therefore in collaboration with the AMANDA and ICECUBE teams we have produced several samples of sources, now in advance of any test for directional coincidence with high energy data, that should be used for checking in the future, and have also described a stacking technique to determine fluxes and or upper limits. Only, when these pre-defined samples confirm any

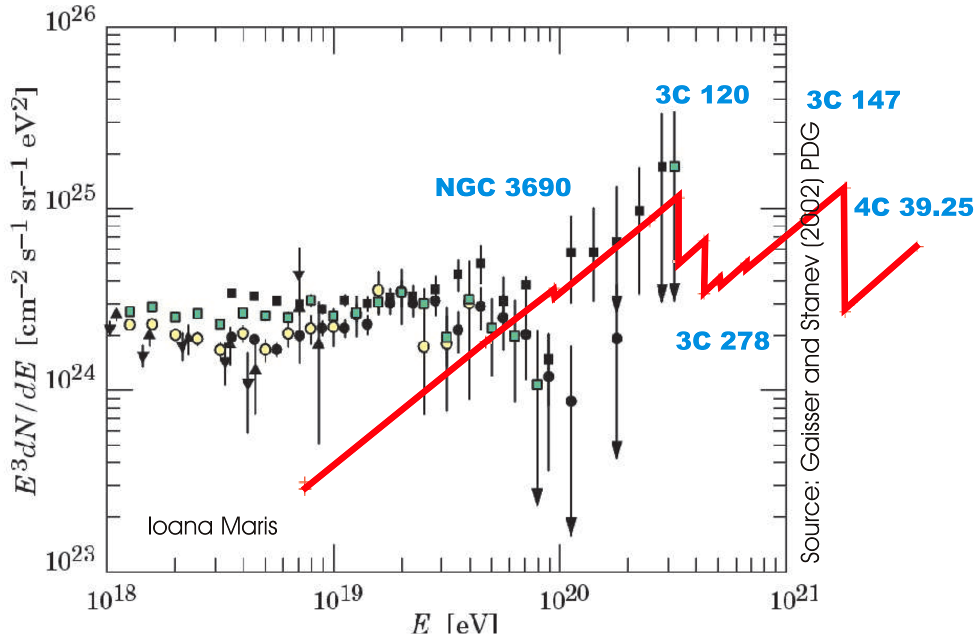

Figure 33: Our predicted spectrum at high energy, from either protons or neutrons with an energy threshold for interaction to the microwave background shifted to higher energy by quantum gravity effects, by sequestering in a fifth dimension, or a unknown particle not interacting with the microwave background. Again we use the predicted flux and maximal particle energy from our physical model for relativistic jets, just with no losses in transit. The data shown are from the various ultra high energy cosmic ray arrays, such as AGASA, HiRes, and earlier experiments, taken from the PDG review by Gaisser & Stanev. The AGASA data suggest an upturn of the spectrum, while the HiRes data suggest a dopwnturn at high energy. It is amazing and gratifying, that famous relativistic sources are picked up by such coincidences, such as 3C147, 3C120, and 4C39.25 - and they could explain the flux of AGASA.

association beyond any doubt, can we be sure that the association is actually real. Only predictions made before any definitive measurements are made, can be tested with some confidence. These predictions could be used for any high energy activity, be it neutrinos, photons, protons, neutrons or other particles, and so ought to be useful also for AUGER, HiRes, EUSO, MAGIC, HESS, Cangaroo and VERITAS.

Here we have shown that there is no plausible association of any cosmic ray event with any known source; on the other hand, we suggest, that the various candidates could be used to develop toy models, to make predictions that in turn will be tested with future data. However, somewhat surprisingly, the flux estimates and particle energies made for just those sources identified by positional coincidences on the sky lead to an unexpected result, see the figure: Those sources, such as 3C147 and 3C120, et alia, do give a possibly sufficient contribution to explain at least a part of the high energy cosmic spectrum observed. Obviously, this is with the very important caveat, that we find a reasonable physical picture to explain the transport of neutrons, neutrinos or some other as yet unknown particle straight across the universe to us. For neutrons effects of Lorentz Invariance Violation - an effect of quantum gravity - could be invoked, for neutrinos we would require a cosmologically local interaction such as the Z-resonance discussed by some, to turn such particles back into hadrons. Other particle physics ideas are being explored, such as sequestering in a fifth dimension, which could be influenced close to the merger of two black holes, a common episode in the activity of black holes in the universe.

→ Becker et al. (2005), Duţan & Biermann (2004), Duţan & Biermann (2005), Wick et al. (2003)

4.5 Dark Matter: A Solution?

It has been shown by Kusenko (Int. J. of Mod. Phys. D, 13, 2065, 2004), that a sterile neutrino in the mass range 2 - 20 keV can explain the *kicks pulsars experience* at birth, giving them linear velocities along their rotation axis up to 1000 km/s. This is a common occurrence in the explosions of massive stars.

It has been shown by by Abazajian et al. (ApJ, 562, 593, 2001), and in Mapelli & Ferrara (MNRAS submitted, astro-ph/0508413, 2005) that the *X-ray background* observations give a constraint for a sterile neutrino mass, with one range allowed to be $\lesssim$ 14 keV, derived from its various decay channels. Much of the X-ray background is actually believed to derive from active galactic nuclei, and the limit of 14 keV could be constrained by improved models for this specific activity.

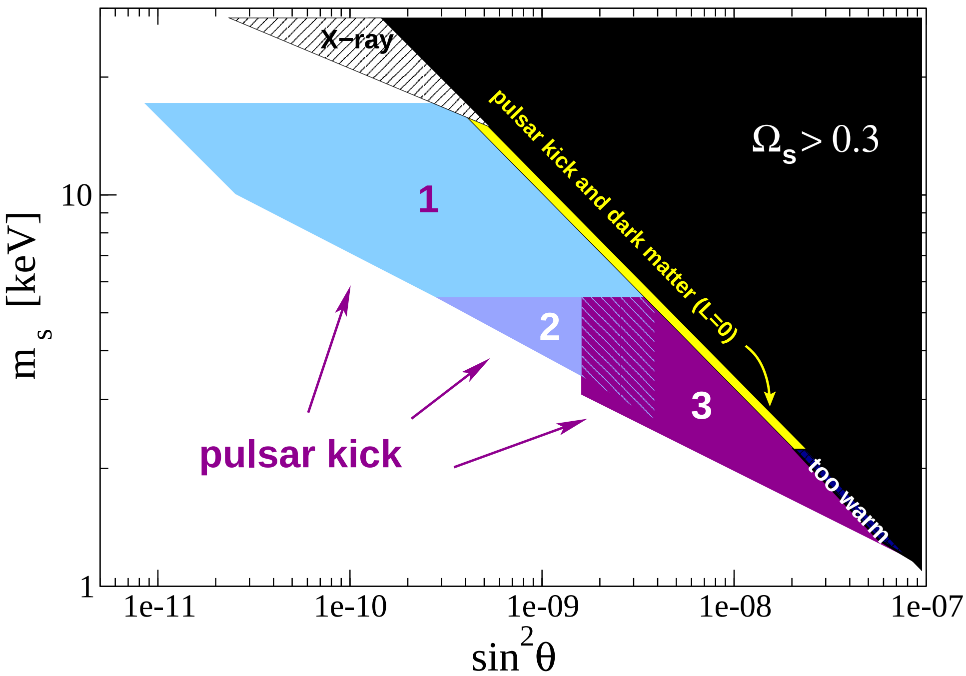

Figure 34: The dark matter particle mass versus its decay mixing angle, showing the various constraints; this figure has been shown in an earlier version by Kusenko, 2004. In order to explain all dark matter, the particle must lie on the diagonal line; its properties are then limited from above by the X-ray background, so < 14 keV, and from below by the mass of the black hole in our Galactic center, so > 10 keV.

It is well known, Bertone, Hooper, & Silk, (Phys. Reports, 405, 279, 2005), that *large scale structure formation* allows a window for a particle below 50 keV. Given the mass of near 12 keV leads to an argument on the smaller scales in large scale structure formation.

We have shown that a Fermion dark matter particle far out of creation-destruction statistical equilibrium in its distribution can explain the *early growth of black holes*, provided the mass range is 12 - 450 keV. The lower mass is given by the mass of the central black hole in our Galaxy, and so allowing for error bars could be as low as 10 keV. This connects to the range of possible activities of central black holes in galaxies.

All these lines of reasonings can be summarized in the statement that a *sterile neutrino of a mass of* 12 ± 2 *keV with a small mixing angle* ($\sin^2\theta \simeq 3\,10^{-10}$) in its decay to an active neutrino is a possible dark matter candidate, see the figure. It appears to fit all observations. Further checks and specific predictions will center on the lowest mass of central black holes in galaxies, expected to be around $2\,10^6$ to $3\,10^6$ solar masses, the highest redshift of quasar activity, expected to be around 10, and large scale structure formation. A consequence would be that the reionization at high redshift has to be caused by the ultraviolet radiation field of massive stars. Another prediction is a broad emission line at exactly half the sterile neutrino mass, so somewhere in the range 5 to 7 keV, which may or may not have been measured already; the published ASCA and CHANDRA data are not conclusive.

→ Biermann (2005), Munyaneza & Biermann (2005)

People involved in Bonn: L. Ancu, P.L. Biermann, A. Bogdan, L. Caramete, S. Casanova, S. Chiţă, V. Curtef, A. Curuţiu, I. Duţan, S. Ghosh, P.-G. Isar, T. Kellmann, I. Mariş, S. Markoff, A. Meli, F. Munyaneza, O. Nenestyan, A. Ødegård, G. Păvălaş, A. Popescu, S.-A. Roman, O.-F. Taşcău, F. Tabatabaei, R. Ulrich, V. Tudose.

Collaborations: J. Becker (Univ. of Dortmund), G. Bisnovatyi-Kogan (Acad. Science, Moscow), H. Blümer (FZ Karlsruhe), Z. Cao (IHEP, Acad. Science, Beijing & Univ. of Utah), M. Chirvasa (MPI for Grav. Phys., Potsdam), A. Donea (Monash Univ., Australia), R. Engel (FZ Karlsruhe), T. Enßlin (MPI Astrophysics, Munich), H. Falcke (Univ. of Nijmegen, Netherlands), P. Frampton (Univ. Chapel Hill, USA), C. Galea (Univ. of Nijmegen, Netherlands & FermiLab, Chicago), A. Gross (Univ. Dortmund), N. Ikhsanov (IoA Cambridge), K.-H. Kampert (Univ. of Wuppertal), H. Kang (Pusan Nat. Univ., Korea), G. Krishna (Nat. Center for Radio Astron., Pune, India), P. Kronberg (Univ. of Toronto, Canada & Los Alamos Nat. Lab., USA), A. Kusenko (UCLA, USA), N. Langer (Univ. of Utrecht, Netherlands), H. Lee (Chungnam Nat. Univ., Daejeon, Korea), K. Mannheim (Univ. Würzburg), G. Medina-Tanco (Univ. of Sao Paolo), S. Moiseenko (Space Research Inst., Moscow), B. Nath (Raman Res. Inst., Bangalore), J. P. Ostriker, (Princeton Univ., USA), R. Protheroe (Univ. of Adelaide), G. Pugliese (ESO, Munich), R. Rezaei (Univ. Freiburg), W. Rhode (Univ. of Dortmund), D. Ryu (Chungnam Nat. Univ., Daejeon, Korea), E.-S. Seo (Univ. of Maryland, USA), R. Sina (Univ. of Maryland, USA), T. Stanev (Bartol Res. Inst., Newark, USA), S. Ter-Antonyan (Inst. for Nucl. Phys., Erewan, Armenia), G. Thomson (Rutgers, USA), A. Vasile (Institute for Space Science, Bucharest), Y. Wang (Purple Mountain Obs., Acad. of Science, Nanjing, China), Feng Yuan (Acad. Science, Shanghai), C. Zier (Raman Res. Inst., Bangalore).